BRNO UNIVERSITY OF TECHNOLOGY

Faculty of Mechanical Engineering

MASTER'S THESIS

Brno, 2023 Bc. Beáta Idesová

BRNO UNIVERSITY OF TECHNOLOGY

VYSOKÉ UČENÍ TECHNICKÉ V BRNĚ

FACULTY OF MECHANICAL ENGINEERING

FAKULTA STROJNÍHO INŽENÝRSTVÍ

INSTITUTE OF PHYSICAL ENGINEERING

ÚSTAV FYZIKÁLNÍHO INŽENÝRSTVÍ

DESIGN AND FABRICATION OF DIELECTRIC METASURFACES FOR ULTRAVIOLET WAVELENGTHS

NÁVRH A VÝROBA DIELEKTRICKÝCH METAPOVRCHŮ PRO ULTRAFIALOVÉ VLNOVÉ DÉLKY

MASTER'S THESIS

DIPLOMOVÁ PRÁCE

AUTHOR — Bc. Beáta Idesová

AUTOR PRÁCE

SUPERVISOR — Ing. Filip Ligmajer, Ph.D.

VEDOUCÍ PRÁCE

BRNO 2023

BRNO UNIVERSITY OF TECHNOLOGY
FACULTY OF MECHANICAL ENGINEERING

Assignment Master's Thesis

Institut:	Institute of Physical Engineering
Student:	**Bc. Beáta Idesová**
Degree programm:	Physical Engineering and Nanotechnology
Branch:	no specialisation
Supervisor:	**Ing. Filip Ligmajer, Ph.D.**
Academic year:	2022/23

As provided for by the Act No. 111/98 Coll. on higher education institutions and the BUT Study and Examination Regulations, the director of the Institute hereby assigns the following topic of Master's Thesis:

Design and fabrication of dielectric metasurfaces for ultraviolet wavelengths

Brief Description:

Metasurfaces are artificially engineered nanostructured surfaces that can function as a variety of conventional and special optical elements. This thesis should investigate metasurfaces made from materials with wide band gap, such as aluminium nitride (AlN) or hafnium dioxide (HfO_2). These materials have sufficiently high refractive index (2) to efficiently control the phase of light waves while exhibiting very little absorption even at ultraviolet wavelengths. The diploma project will consist of physical deposition of AlN or chemical deposition of HfO_2 and the resulting thin films will be subsequently nanostructured. The resulting prospective building blocks of metasurfaces will then be investigated by experiments and simulations. The knowledge gained during the project can be used to design and fabricate a functional metasurface in the UV region.

Master's Thesis goals:

1. Fabrication of nanostructures made of AlN or HfO_2 and subsequent characterization of their optical properties.
2. Verification of the optical response of the nanostructures by comparison with numerical simulations.
3. Fabrication of a prototypical metasurface for ultraviolet range (e.g. metalens).

Recommended bibliography:

ZHAO, D., et al. Recent advances in ultraviolet nanophotonics: from plasmonics and metamaterials to metasurfaces. Nanophotonics, 2021, 10(9), 2283-2308. ISSN 2192-8606. Dostupné z: doi:10.1515/nanoph-2021-0083

GUO, L., et al. Design of aluminum nitride metalens for broadband ultraviolet incidence routing. Nanophotonics, 2018, 8(1), 171-180. ISSN 2192-8606. Dostupné z: doi:10.1515/nanoph-2018-0151

GABLECH, I., et al. Preparation of high-quality stress-free (001) aluminum nitride thin film using a dual Kaufman ion-beam source setup. Thin solid films, 2019, 670, 105-112. ISSN 0040-6090. Dostupné z: doi:10.1016/j.tsf.2018.12.035

Deadline for submission Master's Thesis is given by the Schedule of the Academic year 2022/23

In Brno,

L. S.

prof. RNDr. Tomáš Šikola, CSc. Director of the Institute	doc. Ing. Jiří Hlinka, Ph.D. FME dean

ABSTRACT

This thesis explores metasurfaces operating at ultraviolet (UV) wavelengths as alternatives to conventional optical elements like lenses or holograms. Metasurfaces offer advantages over traditional optical elements such as a reduced footprint of optical systems or multifunctionality within a single device. We start this work with a literature review devoted to UV metalenses and UV metaholograms. We mainly focus on HfO_2 and AlN material platforms because of their high index of refraction (>2) and low losses down to deep-UV region, and we compare fabrication approaches involving these materials. The most promising fabrication recipes were optimized in the practical part of the thesis: HfO_2 metasurfaces were fabricated using atomic layer deposition into masks pre-patterned by electron beam lithography, while AlN metasurfaces were etched through hard chromium masks. We demonstrated successful fabrication of HfO_2 metalenses made of high aspect-ratio nanopillars with circular cross-sections, while the fabrication of AlN metasurfaces faced challenges, which were thoroughly discussed as well. Characterization of the final HfO_2 metalenses in terms of intensity profiles was done in a custom-made experimental optical setup. The metalenses showed promising performance for the wavelength 325 nm, although slight deviations from the design were observed and are discussed in the context of theoretical calculations. The findings of this work emphasize the importance of thorough optimization for the future fabrication of UV metasurfaces.

KEYWORDS

metasurface, UV metasurface, UV metalens, HfO_2 nanostructures, AlN nanostructures, ultraviolet wavelengths

ABSTRAKT

Tato práce se zabývá metapovrchy, které jsou určeny pro ultrafialové (UV, z anglického ultraviolet) vlnové délky a slouží jako alternativa ke konvenčně používaným optickým prvkům jakými jsou například čočky a hologramy. Výhodou metapovrchů oproti konvenčně používaným optickým prvkům je jejich kompaktní rozměr ale take multifunkčnost, která je v této práci demonstrována zpracovanou rešeršní studií zabývající se metačočkami a metahologramy pro UV vlnové délky. V této práci je kladen důraz na dva různé materiály vhodné pro UV vlnové délky — HfO_2 a AlN, které byly vybrány pro svůj poměrně vysoký index lomu (>2) a nízkou absorpci i pro vlnové délky odpovídající hlubokému UV záření. V práci jsou tyto materiály představeny dva odlišné výrobní postupy, kdy pro HfO_2 se využívá depozice atomárních vrstev do předem rezistových připravených masek strukturovaných pomocí elektronové litografie, zatímco pro AlN se využívá leptání přes chromové nebo rezistové masky. Následně je demonstrována úspěšná výroba metačočky z HfO_2 využívající nanostruktur s vysokým poměrem stran ve tvaru válečků s kruhovým průřezem. Plně funkční metapovrch z AlN se nepodařilo demonstrovat z důvodu nedostatečné optimalizace výrobního procesu. Metačočky z HfO_2 byly charakterizovány v experimentální optické sestavě, která umožňuje měřit intenzitní profil a kdy získané výsledky ukazují schopnost metačoček z HfO_2 fokusovat světlo o vlnové délce 325 nm. V naměřených intenzitních profilech čoček se objevují odchylky, které jsou diskutovány a zdůvodněny na základě teoretických výpočtů. Hlavním výsledkem této práce je optimalizovaný výrobní proces HfO_2 nanostruktur s vysokým poměrem stran, který umožňuje výrobu funkčních metapovrchů pro UV vlnové délky a který bude využit v budoucích projektech zabývajících se výrobou UV metapovrchů.

KLÍČOVÁ SLOVA

metapovrch, UV metapovrch, UV metačočka, HfO_2 nanostruktury, AlN nanostruktury, ultrafialová oblast

IDESOVÁ, Beáta. *Design and fabrication of dielectric metasurfaces for ultraviolet wavelengths*. Brno: Brno University of Technology, Faculty of Mechanical Engineering, Department of Physical Engineering, 2023, 71 p. Master's Thesis. Supervised by Ing. Filip Ligmajer, Ph.D.

Author's Declaration

Author:	Bc. Beáta Idesová
Author's ID:	209505
Paper type:	Master's Thesis
Academic year:	2023/24
Topic:	Design and fabrication of dielectric metasurfaces for ultraviolet wavelengths

I declare that I have written this paper independently, under the guidance of the advisor and using exclusively the technical references and other sources of information cited in the paper and listed in the comprehensive bibliography at the end of the paper.

As the author, I furthermore declare that, with respect to the creation of this paper, I have not infringed any copyright or violated anyone's personal and/or ownership rights. In this context, I am fully aware of the consequences of breaking Regulation § 11 of the Copyright Act No. 121/2000 Coll. of the Czech Republic, as amended, and of any breach of rights related to intellectual property or introduced within amendments to relevant Acts such as the Intellectual Property Act or the Criminal Code, Act No. 40/2009 Coll. of the Czech Republic, Section 2, Head VI, Part 4.

Brno ....

author's signature*

*The author signs only in the printed version.

Velké díky patří především Ing. Filipovi Ligmajerovi, PhD. za odborné vedení mé práce, za jeho čas a nespočet cenných rad, které mi poskytl nejen v průběhu psaní tohoto textu, ale také při stavbě optické sestavy pro měření vzorků a při interpretaci měřených dat. Obzvlášť si cením Tvého přístupu k vědecké práci, Filipe, který je pro mě velkou inspirací. Mé díky také patří Ing. Kataríně Rovenské, která mi kromě mnoha rad týkajících se přípravy vzorků a návrhu designu metačoček poskytla také pevný základ pro práci v laboratoři a byla mi oporou již od mé bakalářské práce. Káťo, jsi už třetím rokem mým velkým vzorem. Ing. Mgr. Peterovi Kepičovi bych chtěla poděkovat nejen za první numerické simulace AlN nanostruktur, ale také za jeho upřímný zájem a ochotu konzultace během psaní této práce. Také bych chtěla poděkovat Ing. Imrichovi Gablechovi, PhD. za přípravu AlN vrstev pro následné nanostrukturování. Za rady týkající se depozice atomárních vrstev do rezistových masek, tvorby designu metapovrchů a také konzultace teoretických výpočtů děkuji Ing. Ondřejovi Červinkovi. Za vysvětlení základních principů numerických simulací a za pomoc s interpretací jejich výsledků děkuji nejen Filipovi a Peterovi, ale také Ing. Martinovi Hrtoňovi, PhD.. Také bych chtěla poděkovat za přátelské pracovní prostředí spolupracovníkům v laboratořích CEITEC Nano a za přínosnou diskuzi nad výsledky členům naší plazmonické skupiny. Dannymu, Pavlovi a Míši děkuji za skvělou atmosféru při psaní. V neposlední řadě bych také chtěla poděkovat své rodině a přátelům, zejména Barunce a Jirkovi, za podporu nejen během psaní této práce. Bez nich by tato práce jen těžko vznikla.

Tato práce byla provedena za podpory výzkumné infrastruktury CzechNanoLab (ID LM2023051, MŠMT, 2023–2026), CEITEC Vysoké učení technické v Brně.

Contents

Introduction

Conventional optical elements manipulate incident light by gradual phase shifts acquired via propagation through media of a higher index of refraction than surrounding environment. This approach makes these optical elements bulky, which goes against the miniaturization trends experienced in recent years. The first steps towards miniaturization were done already in the 19th century with the design of so-called "Fresnel lens" [1], which is based on the diffraction theory and together with other diffractive optical elements presents an intermediate step in the history of miniaturization of optical components. In recent years, nanophotonics introduced metasurfaces, which are able to manipulate light at the subwavelength scale, leading to new opportunities in the design and fabrication of optical devices. Unlike their conventional counterparts, metasurfaces are composed of subwavelength structures, so-called meta-atoms, which can be tailored to manipulate the amplitude, phase, and polarization of the incident light, enabling creation of compact and high-performance optical devices [2]. Metasurfaces can operate at a wide range of wavelengths, from the infrared ones down to the ultraviolet ones, while the characteristic dimensions of the meta-atoms are scaled down proportionally to the wavelength of the incident light. The main goal of this thesis is to design and fabricate a metasurface employing HfO_2 or AlN meta-atoms and demonstrate their performance via a functional sample, such as a metalens.

Chapter 1 describes the main operational principles of metasurfaces based on the material which forms the meta-atoms. The main emphasis is put on the dielectric metasurfaces, which have great potential in optics due to their low absorption. The phase manipulation mechanisms, as well as their application in devices, such as metaholograms and metalenses, is described.

Chapter 2 introduces ultraviolet (UV) light and its applications in industry and in everyday life. The emphasis is put on the tight limitations associated with manufacturing conventional optical elements for UV wavelengths. This introduction is followed by a description of new material platforms used in metasurface fabrication, both from the oxide (HfO_2, Nb_2O_5, Ta_2O_5) and from the nitride family (AlN, Si_3N_4). The chapter is concluded with a review of UV metasurfaces, listing the results achieved so far in terms of materials used for the fabrication of functional samples or in terms of theoretically proposed metasurface designs.

Chapter 3 begins with finite-difference time-domain simulations done to estimate the optical response of HfO_2 and AlN meta-atoms. These simulations are crucial for the metalens design, which is described as well. After the simulations, we describe general principles of techniques used for fabrication of the HfO_2 and AlN metasurfaces. In the rest of the chapter the main focus

is drawn to the fabrication optimization of HfO_2 meta-atoms, where HfO_2 is deposited using atomic layer deposition into a polymer mould prepared by electron beam lithography. This approach allows for fabrication of very precise high aspect-ratio nanostructures, which is demonstrated on functional samples of a 5-level HfO_2 metalens. The chapter is closed with a description of a custom optical setup that utilizes a 325 nm wavelength light source and allows for scans of the intensity profiles behind metalenses. For thorough description of steps taken towards optimization of AlN meta-atoms, see Appendix A.

Chapter 4 presents measured intensity profiles of functional 5-level metalenses acquired using the custom optical setup. The results are discussed and compared with the relevant theoretical calculations. Based on this comparison, several conclusions are drawn regarding the position of focal points and fabrication precision of the fabricated metalenses.

Overall, this work aims to advance our understanding of the optical properties and fabrication possibilities of nanostructures made of AlN or HfO_2, and to demonstrate the potential of UV metasurfaces by means of thorough literature review about UV metalenses and metaholograms. Moreover, this work provides an optimized fabrication process for metalens fabrication, as well as theoretical calculation-based discussion related to their functionality.

1 From conventional optical elements to metasurfaces

In the latest years, great focus has been drawn to miniaturization in the technological industry, presenting new fabrication challenges that lead to finding new ways how to make conventionally used elements smaller, better, multifunctional, and more reliable. In the optical industry, it is not different. This industry is faced with a great task — overcoming bulky, heavy, dispersive and absorptive conventionally used optical elements and replacing them with an attractive solution that would allow for implementation in novel optical systems smaller than ever. The miniaturization of the conventional optical elements happened well before the existence of nanosciences in the 19th century when Fresnel lenses were used in lighthouses [1]. Fresnel lens, as can be seen in Figure 1.1, acts as a conventional lens, except instead of phase accumulation from 0 to multiple magnitudes of π, it forms a step-profile, which varies the phase only from 0 to 2π, which is sufficient for complete light manipulation. Nowadays, nanophotonics offers a promising solution in a form of metasurfaces which are able to modify the amplitude, polarization and phase of the incident light with more degree of freedoms and far more precisely compared to the Fresnel lenses [3] by engineering the building blocks out of which the metasurface is made. These building blocks are usually arranged in arrays, which occupy as little as units of micrometres squared. Metasurfaces can also play a role of multifunctional elements, allowing for example for simultaneous filtering and focusing within one element raising the spatial efficiency of such systems even more. The mechanisms which make such manipulation of the

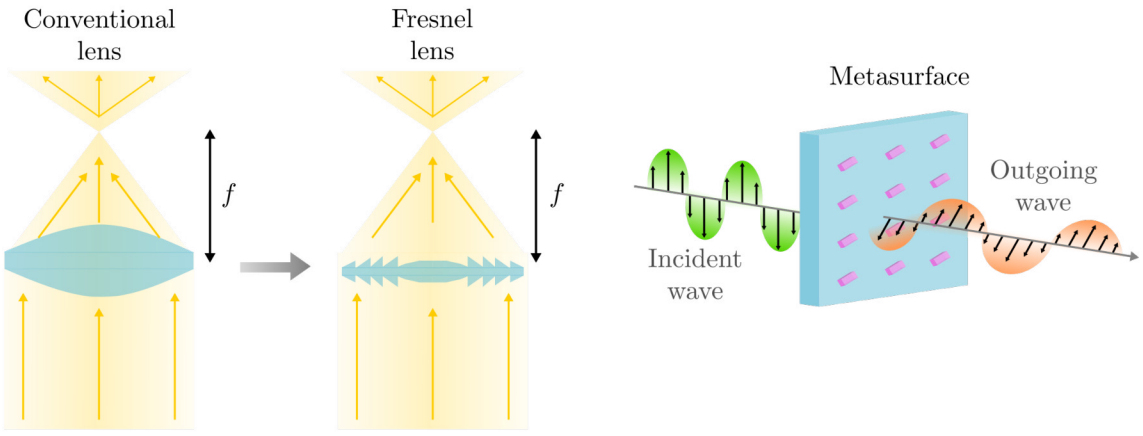

Fig. 1.1: Schematics of the first steps towards miniaturization of the optical elements: From a conventional bulk glass lens through the intermediate case represented by Fresnel lens down to a modern solution offered by nanophotonics in a form of metasurfaces, which are capable of manipulating an amplitude, polarization and phase of the incident light.

incident light by the metasurfaces possible are crucial and will be in principle discussed in the next section.

1.1 Metasurfaces

Metasurfaces are two-dimensional nanostructured surfaces composed of so-called meta-atoms. By controlling the shape, size, and relative position of these meta-atoms using novel nanotechnology fabrication techniques, it is possible to form metasurfaces whose properties can not be found in nature, but whose existence is not restricted by Maxwell's equations [4]. The response of the metasurface to the impinging electromagnetic field is strongly bounded to the dielectric function of materials used in the fabrication of a given metasurface. The dielectric function is a complex function whose real part describes the polarization of the material resulting in lowering of phase velocity of the incident electromagnetic field and the imaginary part corresponds to the absorption in the material. Based on the material to which the impinging electromagnetic field is coupled, we can distinguish between metallic and dielectric metasurfaces.

1.1.1 Metallic metasurfaces

In metallic metasurfaces, the incoming electromagnetic field is coupled to oscillations of the free electron gas in each metallic meta-atom which can be understood as an oscillation of an electric dipole $\boldsymbol{p}$ shown in Figure 1.2a. These oscillations are called localized surface plasmons (LSP) and their resonant frequencies are not only dependent on the dielectric function of the metal and surrounding media but also on the geometry of the meta-atom. In order to excite LSP, the real part of the dielectric function must be negative which is possible only for frequencies corresponding to plasma frequency of the given material and lower, leaving only a limited window of possible excitations [5]. In general, the imaginary part of the dielectric function of metals is not negligible, leading to Ohmic losses in metallic media. As the dielectric function is wavelength-dependent, so is the absorption performed by metallic nanostructures. This finds its use in biological and chemical sensing where absorption on specific wavelengths is crucial [2]. However, considering optical applications, the number one requirement is to keep the absorption of the electromagnetic field in the metasurface as low as possible. Hence, metallic metasurfaces do not seem to be the best material option. Another important factor is the freedom in the manipulation phase of the incident light in the whole 2π interval. In metallic nanostructures, one finds that LSP resonances can be approximated as harmonic oscillators whose phase shifts cannot in principle exceed π by

varying only its characteristic frequency as noted in [2]. The basic principle was explained by M.Kats *et al.* [6], who describe a model of LSP as harmonic oscillator driven by the applied field $E_0 e^{i\omega t}$ on the charge q located at $x(t)$ and mass m with spring constant κ (presenting elastic constant of the restoring force) by the equation

$$m\frac{d^2x}{dt^2} + \Gamma_a\frac{dx}{dt} + \kappa x = qE_0 e^{i\omega t} + \Gamma_s\frac{d^3x}{dt^3}. \tag{1.1}$$

Aside from the internal damping force noted as $\Gamma_a\frac{dx}{dt}$, there is so-called Abraham-Lorentz recoil force $\Gamma_s\frac{d^3x}{dt^3}$ which is the damping force the charge experiences when emitting radiation. If we consider the harmonic motion $x(\omega, t) = x_0 e^{i\omega t}$, the solution is found as

$$x(\omega, t) = \frac{(q/m)E_0}{(\omega_0^2 - \omega^2) + i\frac{\omega}{m}(\Gamma_a + \omega^2\Gamma_s)} e^{i\omega t}, \tag{1.2}$$

where the $\omega_0 = \sqrt{\frac{\omega}{m}}$. In this solution, the oscillations' amplitude is in phase with the driving field for $\omega \to 0$, however, for $\omega \to \infty$, the amplitude's phase shifts by π [2] but no more. This presents another limitation in employing metallic nanostructures in the optical application unless the resonant modes of anisotropic nanostructures are employed [7]. On the other hand, in dielectric media the imaginary part of the dielectric function is much lower compared to the metallic materials and the induced phase can cover the whole range of 2π. Hence, dielectric materials are more suitable candidates for optical non-absorbing applications.

1.1.2 Dielectric metasurfaces

The response of dielectric metasurfaces to an incoming electromagnetic wave is based on excitation of so-called Mie resonances. In the simplest case for a dielectric nanoparticle, as depicted in Figure 1.2a, we distinguish between the first Mie resonance which corresponds to the oscillation of a magnetic dipole $\boldsymbol{m}$ and the second Mie resonance which corresponds to the oscillation of an electric dipole $\boldsymbol{p}$ [8]. The resonant response of magnetic dipoles is a result of coupling of the incident electromagnetic wave to circular displacement currents of the electric field induced in the dielectric [9]. Let us consider a high-index dielectric sphere of diameter d illuminated by a plane wave of wavelength λ. In order to excite both of the Mie resonances, condition $d \approx \lambda/n_{\text{diel}}$ (where n_{diel} is the refractive index of the dielectric at the given wavelength) must be fulfilled [9]. The possibility of exciting magnetic dipoles in dielectric metasurfaces leads to a significant enhancement of scattering efficiency even in dielectrics exhibiting low absorption. As discussed in the previous Section 1.1.1, aside

from low absorption, another key factor is the freedom in the manipulation of the incident light in the whole range from 0 to 2π. In the dielectric nanostructures there are several mechanisms that enable covering the whole 0 to 2π phase and hence allow for achieving greater freedom in light manipulation than metallic nanostructures.

We distinguish between several groups of dielectric metasurfaces based on the key mechanism through which the phase shift is acquired in dielectric nanostructures — propagation phase, geometric phase and electromagnetic resonance phase. Schematics of the metasurfaces employing these mechanisms are shown in Figure 1.2b. The propagation phase shift is based on waveguide modes propagating through the building blocks of varying height. Therefore, the propagation properties highly depend on the size and shape of the meta-atoms. Such meta-atoms act as truncated low-quality Fabry-Pérot resonators, each supporting different effective refractive indices [10]. The next group, where the phase shift is acquired through orientation anisotropy of nanostructures, exploits so called Pancharatnam-Berry or geometric phase, and are accordingly called geometric phase metasurfaces [11]. The performance of the last group of dielectric metasurfaces, the electromagnetic resonance-based ones, is entrenched in excitations of electric and magnetic Mie dipoles. To achieve the whole 2π phase change of the incoming light, both electric and magnetic dipoles need to be excited simultaneously in the meta-atoms, since each of the dipoles induces the phase shift of π. In case we are able to excite both magnetic and electric resonance inside a dielectric nanostructure, and these resonances spectrally overlap, we can speak of the so-called Huygens' source [10]. Huygens' sources provide high transmission efficiency and directionality since there is zero backward scattering due to the destructive interference of magnetic and electric multipole coefficients, resembling what Kerker *et al.*

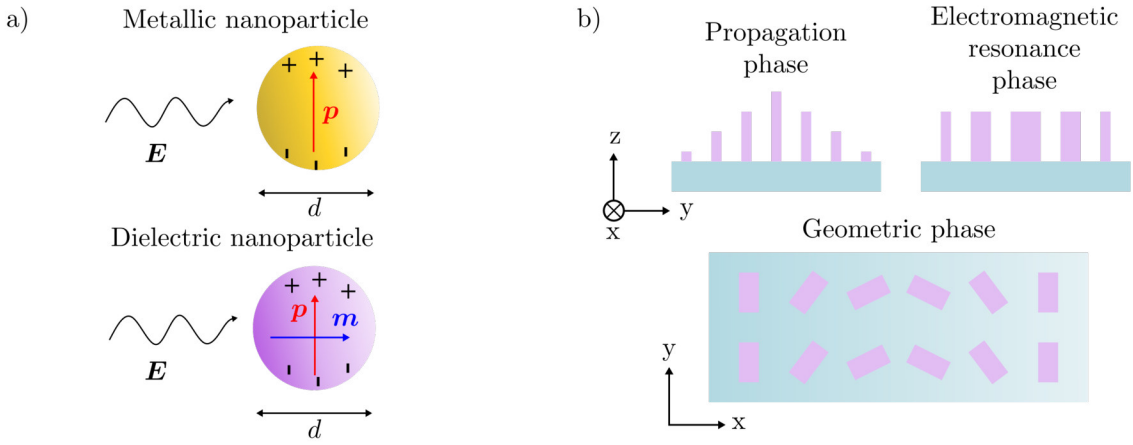

Fig. 1.2: a) Comparison of the excitations of electric dipole $\boldsymbol{p}$ and magnetic dipole $\boldsymbol{m}$ oscillations in the metallic and dielectric nanoparticle of diameter d by the incident field $\boldsymbol{E}$. b) Schematics of phase-acquiring mechanisms in dielectric metasurfaces.

suggested happens in spheres made of a material in which relative electric permittivity and relative magnetic permeability are equal [2, 12]. In such case, the dielectric particle behaves as a unidirectional source of light, resembling a Huygens point source. In most dielectric metasurfaces, phase manipulation is usually achieved via an interplay between multiple phase-acquiring principles, which ensures the freedom of phase manipulation, allowing for imitating complex phase profiles of various optical elements.

Many interesting applications such as metalenses [13], beam deflectors [14], polarization beam splitters [15] and metasurfaces allowing for colour printing [16], polarization manipulation [17] or beam steering [18] have been proposed. In the following section, the basic principle of metaholograms and metalens will be discussed.

Metaholograms

Holography, from the most general viewpoint, allows for three-dimensional optical reconstructions of real-world objects. It is based on interference between the object and reference wavefronts forming an interference pattern. Once the interference pattern is later illuminated by the reference beam again, we are able to reconstruct the impression of the object that was illuminated by the target beam in the first step [19]. Nowadays, we usually do not rely on physical objects but rather on generating interference patterns via theoretical optical computations — also referred to as computer-generated holography (CGH) [20]. Conventional holograms are limited due to the lack of narrow bandwidth, multiple orders of diffraction present, twin images and other limitations [21]. These are present due to the spatial resolution of conventionally used spatial light modulator, which causes degradation of the reconstructed image, as well as due to the limited resolution of the conventional media recording the interference pattern. With the availability of the interference patterns of virtual objects using CGH, it is possible to mimic such interference patterns with nanostructures and hence construct metaholograms. Metaholograms provide better spatial resolution and precision of the reconstructed images with low noise and elimination of unwanted diffraction orders, owing to the subwavelength sizes of the nanostructures [21].

In general, we distinguish between phase-only, amplitude-only and complex holograms, depending on whether the phase, amplitude or both are recorded [21]. These are possible to make even with conventional optical elements, however, in the sense of miniaturization, the multifunctionalities of the metasurfaces are of great interest, because they can implement multiple optical elements in one compact surface. Metasurfaces allow for so-called holographic multiplexing, which is possible because properties of light, such as the direc-

tion of propagation, wavelength and polarization, can be manipulated independently. One of the possibilities is the polarization-multiplexing metahologram, whose design is based on anisotropic nanostructures (for example nanobricks with rectangular cross-sections) operating as half-wave plates, which convert left-handed circularly polarized (LCP) light to right-handed circularly polarized (RCP) light employing the geometric phase as was mentioned earlier in this chapter [22]. In order to maximize the conversion efficiency of LCP to RCP, the metasurface must perform high transmissivity for both orthogonal electric field components, as well as phase delay π between them ensuring the conversion. The high transmission of a metasurface is achieved because of the simultaneous excitation of both magnetic and electric dipoles, as well as due to the low absorption of the given wavelength for the material used. The phase shift of π acquired by the transmitted wave can be explained via a model which takes into consideration the excitation of antiferromagnetic resonant modes induced by circularly polarized light [23]. In this model, the incident light induces antiparallel magnetic dipoles in the volume of the nanostructures. For the geometry of the nanobrick that acts as a half wave plate inducing the change of π, we expect an even number of modes to be excited in the volume of the nanobrick along the short side of the nanobrick and an odd number of modes along the long side. Once we illuminate such structure, the component of the electric field E_x perpendicular to the short side remains unchanged, while the component E_y perpendicular to the long side is changed in phase by π, which is schematically shown in Figure 1.3. A good way to quantify the performance of a metahologram is by its efficiency, which is measured as the ratio between the total power enclosed by the holographic image to the total power of the incident light illuminating the metahologram. With the

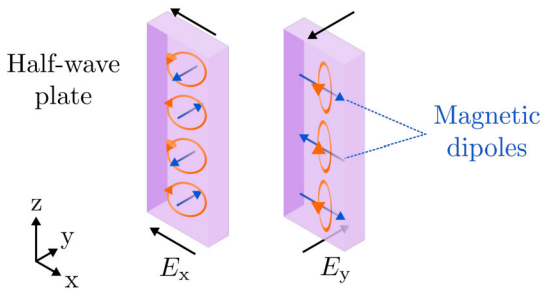

Fig. 1.3: Schematics of a nanostructure which functions as a half-wave plate. The excitation of antiferromagnetic resonant dipoles allows for control of the polarization of the incident electromagnetic wave. For the odd number of excited magnetic dipoles, the phase of the given component of the electric field is shifted by π. E_x and E_y are components of the incident electromagnetic wave marked by black arrows, red arrows correspond to the displacement currents which induce magnetic dipoles noted by blue arrows.

above mentioned introduction to metaholograms and their functionality, the following text will take a closer look at metalenses.

Metalens

Conventional lenses present the essential components of the optical system and their properties affect the final quality of the image the most. Those lenses are usually based on gradual accumulation of phase during the propagation of light through glass, which is ensured by the surface topography [24]. The problem of bulky conventional optical systems could be solved in an elegant way by implementing metasurfaces not only for their compact size in term of thickness but also for the possibility to develop devices of outstanding performance and functionality compared to their conventional counterparts [24]. Lenses capable of converting incident planar wavefronts into spherical ones have phase profiles given by the following equation [2]:

$$\varphi(x, y) = -\frac{2\pi}{\lambda}(\sqrt{x^2 + y^2 + f^2} - f), \tag{1.3}$$

where λ is the wavelength of the incident light, f is the focal point of the lens and x, y are spatial coordinates of the meta-atoms forming the metalens. In metalenses, this phase profile is not continuous but is split into discrete levels between 0 and 2π, which are consequently covered by dielectric nanostructures of desired phase response caused by one of the previously mentioned mechanisms — by propagation, geometry or electromagnetic oscillations [25]. One way how to quantify the functionality of a metalens is to measure its focusing efficiency which is the ratio between the optical power of the focused spot and the total power that illuminates the metalens. Apart from the simple metalens with a single focal point, it is possible to fabricate multifocal metalenses whose phase profiles become more complex since these lenses form multiple focal points in the focal plane based on the properties of the incident light (such as polarization) as will be discussed in the following chapter in the section related to the dielectric ultraviolet metalenses.

All of the above-mentioned applications are dependent on the wavelengths at which these devices operate. Appropriate materials must be chosen in order to minimize the potential losses caused by absorption due to the interband transitions within the material. For visible and infrared wavelengths, titanium dioxide (TiO_2) [26], silicon (Si) [27], gallium phosphide (GaP) [28], and many more were proposed as suitable materials since they have a big enough band gap that does not allow for absorption at visible and longer wavelengths. TiO_2 seems to be the most widely used material so far, not only for its wide band gap of ca. 3 eV and low absorption of visible wavelengths but also for the fact that TiO_2 allows for very precise fabrication of high aspect ratio nanostructures by

various techniques [29, 30]. Silicon, being widely used in the semiconductor industry, has been used for metasurfaces at infrared wavelengths mainly for its compatibility with complementary metal oxide semiconductor technologies [31]. When dealing with the light of shorter than visible wavelengths, many of these materials become inconvenient for their increasing absorption and new materials with wider band gaps must be chosen, allowing for sustaining as high transmissivity of the optical elements as possible. The next chapter will mainly focus on ultraviolet light and suitable materials and review achievements in terms of fabrication and design of metalenses and metaholograms suitable for ultraviolet wavelengths.

2 Reaching beyond the violet light

The discovery of ultraviolet light dates back to 1801 when Johann Wilhelm Ritter experimented with silver chloride crystals that darkened when exposed to light [32]. Ritter exposed silver chloride to various light wavelengths (colours) using a prism and observed its reactions. Unexpectedly strong darkening of silver chloride was observed not only for the blue and violet colours but also in the region below the violet light, where no visible light was present [33]. That observation led Ritter to a conclusion that there exist rays beyond the violet light – this part of the spectrum is nowadays called ultraviolet (UV) and refers to wavelengths approximately from 10 nm to 400 nm.

2.1 UV spectrum and conventional optical elements

It is possible to differentiate between three types of UV irradiation — UV-A, UV-B and UV-C. These three categories are assigned to different wavelength intervals, as can be seen in Figure 2.1, and are commonly used when referring to the impact of light on living organisms in life sciences or its effect in earth sciences. UV-A, or the "long UV" is the softest non-harmful irradiation, UV-B is responsible for the increased risk of cellular damage in living organisms and finally, the strongest one is UV-C. In technical sciences, we are usually speaking of near-UV, mid-UV, deep-UV, vacuum-UV and extreme-UV [34]. Their corresponding ranges are shown in Figure 2.1 as well.

UV irradiation is used for many purposes such as surface sterilization [35], water disinfection [36], medical treatment [37], communication [38], imaging [39], high-resolution photolitography [40] and many more. For many of these applications, optical components like lenses or polarizers are needed and the shorter the wavelength we use, the tighter the requirements for optical components become in terms of size tolerances and suitable materials. For a lens with standard precision, as stated by Edmund Optics Company [41], peak-to-valley tolerance (describing the flatness of the surface of the lens) must be held at

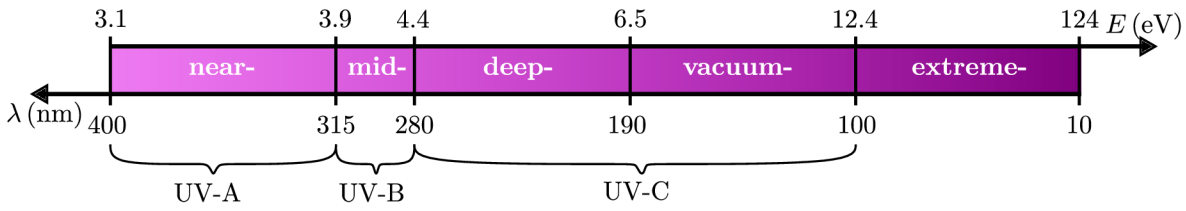

Fig. 2.1: UV spectral ranges based on the narratives of life sciences, and technical sciences and their corresponding wavelengths and energies. Picture inspired by [34].

$\lambda/10$ (where λ is the wavelength of the incident light). To keep the relative distortion of a wavefront low for UV light ($\lambda = 300\,\text{nm}$) with respect to visible light ($\lambda = 600\,\text{nm}$), we need twice as tight irregularity tolerance regarding the precision of the surface of the lens. Apart from the surface flatness, this $\lambda/10$ rule also applies to the precision of the thickness of coatings used for UV lenses. Moreover, surface imperfections of UV lenses become sources of scattering and absorption, thus, reducing the effectivity of the whole optical system. These requirements make the standard approach used in the fabrication of conventional optical elements quite challenging. Besides the tight precision tolerances, the fabrication of UV optical elements is also limited by the availability of suitable materials. A UV-compatible material must have a band gap big enough to transmit the UV light as any possible absorption could lead to bleaching and chemical alteration of the material, and thus to its irreversible damage. The most commonly used materials are sapphire, calcium fluoride and fused silica [41]. Sapphire transmits light down to 150 nm, and is suitable even for harsh conditions due to its hardness. Although it is generally birefringent material, this unwanted effect can be avoided by cutting it along its C-axis [42]. Calcium fluoride transmits light down to 180 nm with intrinsic as well as stress-induced birefringence, which needs to be considered when designing optical setups [43]. Fused silica transmits light down to 193 nm and offers high-temperature stability and radiation resistance [44]. Apart from these three elements, mentioned by Edmund Optics Company, quartz [45], fluorides of magnesium, barium and lithium [46] are used by various optical companies. Besides the limited material range for fabrication, conventional UV lenses also suffer from greater aberrations than their counterparts suitable for visible and infrared wavelengths, mainly due to stronger dispersion of the UV-compatible materials. The presence of aberrations causes the whole optical system to be even bulkier because the necessary correcting elements have to be included.

Based on the aforementioned limitations of conventional optical elements (precision and material requirements), finding new strategies for handling UV light is of great interest. Metasurfaces present a modern solution for this problem not only for their compact size but also for the promising precision of fabrication. In general, it is possible to manipulate the light using suitable geometry and size of the meta-atoms as described in Section 1.1.2. However, this approach still faces the challenge of choosing a material with big enough band gap that the absorption will remain as low as possible at UV wavelengths. We also must note that the limits of techniques used in metasurface fabrication are being tested greatly since the dimensions of the meta-atoms can be as small as tens of nanometres, while their height is in the order of hundreds to. The constrain on the diameter of the nanostructures is set by the Mie resonance

condition discussed in Section 1.1.2, while the height of multiple orders of the nanostructue's diameter is crucial for phase manipulation of the incident light, employing the propagation phase. Some of the proposed metasurface designs are hence still beyond the technical possibilities available nowadays. Metamaterials and metasurfaces suitable for UV wavelengths classified based on their potential applications are summed up in a recent review by Zhao *et al.* [34]. The next section of this chapter will take a closer look at materials suitable for UV region as well as fabrication and simulation achievements from the material point of view, demonstrating the potential of metasurfaces for UV applications but also some gaps that still need to be filled by future research.

2.2 Materials suitable for UV applications

Aside from the materials mentioned in the previous chapter, namely sapphire, calcium fluoride and fused silica, a few more interesting options of the dielectric materials within the oxide and nitride chemical groups were proposed by recent research, which will be discussed in the following text. However, not all of them seem to present viable solutions due to the challenges in fabrication.

In the family of oxides, hafnium dioxide, niobium pentoxide and tantalum pentoxide were proposed as suitable candidates mainly for their large energy bandgaps and high refractive indices, which are summarized in Table 2.1. Hafnium dioxide (HfO_2) is a dielectric material with the largest bandgap out of the mentioned oxides, providing great potential for deep UV applications [47]. Moreover, HfO_2 often serves as an insulating layer in complementary metal-oxide-semiconductor (CMOS) circuits or even in novel photosynaptic devices and neural networks due to its high relative dielectric constant [52], presenting wide variety of the material multifunctionality. Niobium pentoxide (Nb_2O_5) is an interesting material due to its bandgap energy spanning almost 2 eV. This variation is based on the grain size of the deposited oxide as well as its crystalline structure, which are significantly dependent on the temperature during

Tab. 2.1: Materials from the oxide and nitride group suitable for UV wavelengths, their bandgap energies E_g, wavelengths corresponding to bandgap energies λ_g and indices of refraction n and references (Ref.)

		E_g (eV)	λ_g (nm)	n	Ref.
Oxides group	HfO_2	5.7	217	> 2.1	[47]
	Ta_2O_5	4	309	> 2.2	[48]
	Nb_2O_5	3.1– 5.3	234–400	> 2.2	[49]
Nitrides group	AlN	6.11	202	> 2	[50]
	Si_3N_4	5	248	> 2	[51]

the deposition [53]. Subsequent heat treatment or even nanostructuring of the Nb_2O_5 film also affects the energy of the band gap [53]. The last example form the oxide group tantalum pentoxide (Ta_2O_5), covers the near-UV to mid-UV ranges, usually standing in between the two previously mentioned oxides [48].

The nitride group is represented by silicon nitride (Si_3N_4) and aluminium nitride (AlN). Band gaps of both of these materials are 5 eV and 6.1 eV respectively, demonstrating great potential for deep UV applications. (See Table 2.1). Their biggest disadvantage with respect to oxides is the lack of low-temperature fabrication techniques, which are more advantageous for precise fabrication, as will be described in the following text. The next chapters will mainly focus on two particular applications of dielectric metasurfaces, namely metaholograms and metalenses, with the main aim of showcasing fabrication achievements of functional metasurfaces as well as ideas behind complex designs of metasurfaces that are yet waiting to be fabricated. These applications will mostly employ materials mentioned in this section.

2.3 UV metaholograms

For UV wavelengths, polarization-multiplexed as well as polarization-independent metaholograms from six different materials have been reported so far in literature, and their main characteristics are summarized in Table 2.2. As we can see there, most of the reported metaholograms are functional samples. Functional samples from HfO_2 were prepared by Zhang C. *et al.* [47], who reported both polarization-multiplexed metaholograms designed for two different wavelengths as well as polarization-independent metaholograms designed for three different wavelengths, employing nanopillars with elliptical and circular cross-sections, respectively. As can be seen in Table 2.2, the efficiency of all of the prepared metasurfaces from HfO_2 exceeded 50 %. Even higher efficiency was reached by metaholograms formed by Nb_2O_5 nanobricks with a rectangular cross-section [49]. Huang *et al.* fabricated not only a simple metahologram that transforms LCP light to RCP light with efficiency greater than 79 % but also a more complex device that shows three different holographic images based on the polarization of the incident light with efficiency greater than 78 %. Such metahologram which is capable of displaying multiple images based on the characteristics of the incident light was said to have great potential as an anti-counterfeiting device. Another material, Ta_2O_5, used for fabricating functional sample by Zhang C. *et al.* should have a great potential for near-UV and mid-UV applications not only for its wide band gap but also for the possibility to employ the fabrication process, where the layer is deposited first and then etched over a mask as the authors suggest. However, due to not well-optimized etching process, nanostructures do not attain such a high level

Tab. 2.2: Materials proposed for metaholograms based on references (Ref.) — their operation wavelengths, meta-atom cross-sections (C-S) with estimated or measured efficiency depending on if the metahologram was a functional sample or a simulation only (Simul.). Some metahologram's efficiencies were not reported (NR). The meta-atom C-S are marked with symbols — circular ◯, elliptical ⬭ rectangular ▭.

Material	Operation wavelength (nm)	Simul. or Sample	Meta-atom C-S	Efficiency	Ref.
HfO_2	266/364	Sample	⬭	> 53 %	[47]
	266/325/364	Sample	◯	> 60 %	[47]
Nb_2O_5	355	Sample	▭	> 79%	[49]
	355	Sample	▭	> 78 %	[49]
Ta_2O_5	325	Sample	⬭	20 %	[48]
AlN	375	Simul.	◯	∼ 34 %	[54]
Si	355	Sample	▭	NR	[55]
ZrO_2	248/325	Sample	▭	> 48 %	[56]

of precision and hence, the process results in Ta_2O_5 hologram performing only with 20 % efficiency [48]. Based on an AlN material platform, Guo *et al.* theoretically proposed a design of a multi-plane polarization-independent metahologram built from AlN nanopillars with circular cross-section with efficiency of only around 34 % [54]. Lastly, a functional sample targeted at near-UV wavelengths fabricated from rectangular silicon (Si) nanorods was reported by Deng *et al.* [55]. They suggested quite counter intuitive improvement of scattering efficiency due to the employment of absorbing silicon in which enhancement of the imaginary part of the dielectric function corresponding to losses is present. Unfortunately, the measured efficiency of such metahologram was not reported. There was also hybrid-material approach reported by Kim *et al.*, where they demonstrated the functionality of metaholograms for near- and deep-UV with efficiency greater than 48 % [56]. The metasurface meta-atoms are composed of ZrO_2 nanoparticles of 19 nm in nanoparticle-embedded resin (nano-PER), which exhibits a large bandgap of 6 eV, performing low losses for deep-UV wavelengths. Their fabrication approach is based on single-step nanoimprinting of the desired patterns into the nano-PER containing dispersed ZrO_2 nanoparticles, which significantly increases the possible fabrication throughput and therefore has a great potential for mass production.

As can be seen in Table 2.2, most of the mentioned results are based on the functional samples employing not only materials proposed in the Section 2.2

but also Si, whose potential seems to be low at the first glance due to its narrow bandgap 1.11 eV at a room temperature [57], as well as a novel approach of dispersed ZrO_2 nanoparticles in UV-curable resin which allows for nanoimprinting. Samples from HfO_2 and Nb_2O_5 employed the ALD deposition into the resist mask whereas Ta_2O_5 and Si were fabricated via deposition of material onto a substrate as the first step and consequent reactive ion etching over a mask. Finally, AlN metasurface was the only metasurface whose capabilities were proposed based on simulations only.

2.4 UV metalenses

Functional samples and proposed designs for UV metalenses are summarized in Table 2.3. Unlike UV metaholograms, most of the reported results are based on simulations only. A simple metalens for UV was fabricated and measured by Zhang *et al.* [47], employing HfO_2 nanopillars of circular cross-section with a diameter-to-height ratio as high as 11. Even though HfO_2 is generally a material that allows for reaching wavelengths in the deep-UV, they demonstrated

Tab. 2.3: Materials proposed for different types of metalenses based on references (Ref.) — their operation wavelengths, meta-atom type and its cross-section (C-S) with estimated or measured efficiency depending on if the metalens was a functional sample or simulation only (Simul.). Some metalens' efficiencies were not reported (NR). The meta-atom C-S are marked with symbols — circular ◯, elliptical ⬭ rectangular ▭. The MDL stands for multi-level diffractive lens.

Material	Operation wavelength (nm)	Simul. or Sample	Metalens type	meta-atom C-S	Efficiency	Ref
HfO_2	325/364	Sample	Simple	⬭	> 55 %	[47]
	325 - 450	Sample	Multifocal	◯	NR	[58]
AlN	244/ 308/ 375	Simul.	Simple	▭	>29 %	[50]
	244/ 308/ 375	Simul.	Simple and multifocal	▭	> 44 %	[59]
	234 – 274	Simul.	Achromatic	◯	> 38 %	[60]
	244/ 325/ 375	Sample	Simple	Zone plate	> 33 %	[61]
Si_3N_4	300	Simul.	Trifocal	◯ and ▭	NR	[51]
	300	Simul.	Trifucntional	▭	NR	[62]
	250 - 400	Simul.	MDL	—	> 67 %	[63]
	300 - 400	Simul.	Achromatic	◯	> 50 %	[64]
ZnO	394 → 197	Sample	Nonlinear	△	NR	[65]

metalens of focusing efficiency greater than 55 % for the near-UV wavelengths [47]. As a more complex lens, Uenoyama et al. [58] demonstrated a multifocal HfO_2 metalens that served as a part of single-photon avalanche diode arrays and improved the overall performance of a silicon multiplier. The efficiency of such metalens formed by HfO_2 nanopillars with circular cross-section was not reported. The photon detection efficiency of the device with integrated metalens was improved by 50 % in the range of 375-450 nm. In contrast to the HfO_2 material platform, only a zone plate employing AlN as a material of choice was fabricated and reached efficiency greater than 33 % at the near-UV wavelength [61]. This AlN metalens employs theory of zone plates which made the fabrication less precision demanding. Other works from the nitride group are based on simulations only for both AlN and Si_3N_4. Design of AlN metalens composed of nanorods with rectangular cross-sections with an aspect ratio as high as 17 was proposed [50]. Focusing efficiencies of such metalens were estimated below 50 % for all three wavelengths from near-UV to deep-UV region. Another design for AlN metalens was proposed for the same three wavelengths and the same type of nanostructures with slightly improved efficiency 44 % [59]. To cover the range of wavelengths from 300 nm to 400 nm with efficiency greater than 50 %, the simulation of an achromatic metalens employing Si_3N_4 nanopillars with circular cross-sections [64] were done by Butt *et al.* [51]. They proposed an advanced trifocal metalens made of Si_3N_4 nanopillars with circular and rectangular cross-sections with the highest aspect ratio being 12. The multi-functionality of such a lens is based on blending the geometric and propagation phases (see Section 1.1.2), which enables generation of different focusing spots in one focal plane, depending on the incident polarization states. For the same operation wavelength of 300 nm as the metalens designed by Butt *et al.*, another multifunctional metalens design from Si_3N_4 was proposed, using nanopillars with rectangular cross-section, producing multiple focusing spots for different polarizations of the incident light [62]. Lastly, nonlinear metalens was demonstrated by employing ZnO as a material of choice, which allows for converting the impinging light of 394 nm to 197 nm [65]. The design is based on enhanced local nonlinearities in metasurfaces which boosts the conversion efficiency of the incident light and therefore, such mestasurfaces can serve as small generators of light. With the optimized design, the light is not only generated but also focused at the same time, serving as a nonlinear metalens. Compared to the previous works, this nonlinear metalens employs triangular meta-atoms with low aspect ratio where the thickness is only 150 nm and sides of the triangle are 205 nm. Such low aspect ratio nanostructures allowed for a fabrication approach, where the ZnO layer is grown within the first step and is patterned via etching later. The focusing efficiency of such a metalens was not reported.

As summarized in Table 2.3, for the largest part of we were dealing with ambitious proposals of designs that promise great potential for future applications. As mentioned in Section 2.2, at this moment, the prototypes are mostly limited by the lack of precise fabrication techniques that would not limit the deposition temperature to roughly 100 °C and that would allow for the fabrication of nanostructures with smooth sidewalls and high aspect ratios as were demonstrated in works employing HfO_2 [47] and Nb_2O_5 [49]. This problem could be solved by optimization of etching processes, allowing for high temperature depositions as the first step of fabrication and subsequent directional etching over a mask.

The results mentioned so far were not the only metasurfaces fabricated and proposed for UV wavelengths. Designs of metasurfaces producing or detecting vortex beams were proposed for Nb_2O_5 [66, 67] and Si_3N_4 [68–70] material platforms. Two different functional metasurface fabricated from multilayers of ZnS, GeSbTe and SiO_2 [71]. A TiO_2 Huygen's metasurface [72] was demonstrated. Another simulations employing TiO_2 in a wire grid polarizer [73] and diamond nanostructures in Huygens' metasurface [74] were proposed. At this point, most of the metasurfaces suitable for UV wavelengths were summarized in the previous text and divided into two categories (metaholograms and metalenses) based on their functionality. Throughout this chapter, the need for improvement in terms of fabrication techniques and optimization of fabrication processes was stressed out in Sections 2.3 and 2.4.

Based on the review done in this chapter, this work is focused on HfO_2 and AlN material platforms which were chosen for their their wide band gap, making them suitable for deep-UV applications. Fabrication of metasurfaces from these materials as well as verification of their functionality will be demonstrated.

3 Methods

This chapter discusses finite-difference time-domain (FDTD) simulations done to estimate the optical response of the HfO_2 and AlN meta-atoms. These simulations are crucial for the metalens design, which will be demonstrated as well. This section is followed by introduction of the main fabrication techniques, which were used to fabricate the final samples, namely electron beam lithography electron beam evaporation, ion beam sputtering and atomic layer deposition as well as dry etching techniques employing ions. These techniques are crucial for metasurface fabrication. Finally, the custom optical setup used for sample measurements is be described.

3.1 FDTD simulations and metalens design

Before the fabrication itself, FDTD simulations are needed to estimate the parameters of the nanostructures, which will allow the freedom in phase control of the incident light — the induced phase change will cover the full range from 0 to 2π. For this purpose, a set of simulations of meta-atom was performed in Ansys Lumerical FDTD software. The simulated meta-atoms on the SiO_2 substrate were nanopillars with circular cross-sections whose diameter and height could vary. Such a nanopillar is depicted in Figure 3.1a, where D is its diameter, H is its height and P is the spacing between the adjacent nanopillars. The preview of the simulated meta-atom in the software can be seen in Figure 3.1b. The simulation region has periodic boundary conditions set in the x and y directions, and perfectly matched layers set above and below the nanostructure. The perfectly matched layers are absorbing layers which minimize the reflection on the boundary of the simulated region. The

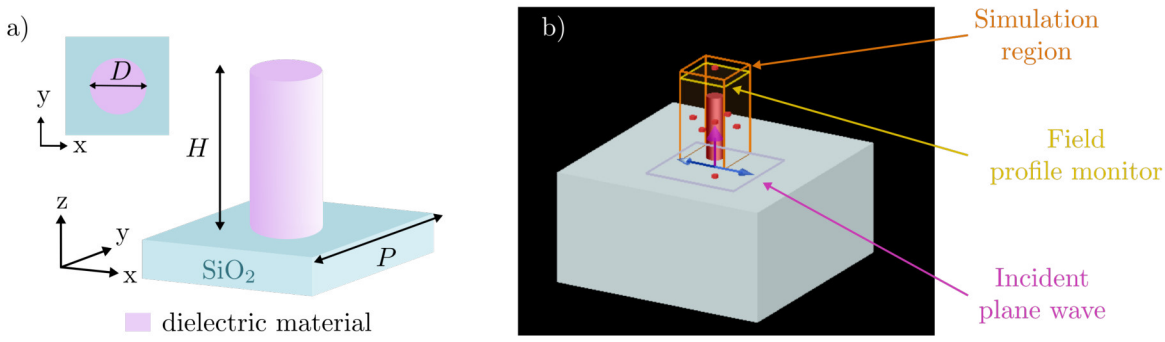

Fig. 3.1: a) Schematics of the simulated meta-atom – nanopillar with circular cross-section of diameter D, height H on the SiO_2 substrate. Nanostructure is in periodic boundary conditions, where the spacing between the adjacent nanostructures is P. b) Preview of the simulated nanostructure in the Ansys Lumerical FDTD software.

nanopillar is illuminated by a plane wave, and the field profile monitor is placed above the nanopillar for the calculation of the induced phase change. This monitor records all vector components of the output electric field $\boldsymbol{E}$ which are then used for calculation of the phase induced by the nanopillar to the incident wave. In general, the output electric field $\mathbf{E}$ propagating through the monitor is given by the Fourier transform:

$$\boldsymbol{E}(k_\mathrm{x}, k_\mathrm{y}) = \iint_S \boldsymbol{E}(x, y)\mathrm{e}^{-i\boldsymbol{kr}}dxdy, \tag{3.1}$$

where $\boldsymbol{k} = (k_\mathrm{x}, k_\mathrm{y})$ is the wave vector in plane of the monitor, $\boldsymbol{r}$ is the position in the area of the monitor and S is the area of the monitor. The information about both the amplitude and phase of the outgoing wave is given by the zeroth component $\boldsymbol{E}(0,0)$ which is normalized to the area S over which it was integrated and is calculated as follows:

$$\boldsymbol{E}(0,0) = \boldsymbol{E}_0 = \frac{1}{S}\iint \boldsymbol{E}(x, y)dxdy. \tag{3.2}$$

The real part of $\boldsymbol{E}_0$ corresponds to the amplitude of the zeroth outgoing component of the electric field and the imaginary part contains the phase ϕ as $\mathrm{Im}\{\boldsymbol{E}_0\} = \mathrm{e}^{i\phi}$.

In order to perform the simulations, optical responses of the used materials are needed. Both the AlN and HfO_2 were characterized via ellipsometry. Ellipsometry is a characterisation technique which allows for investigation of the optical properties of the observed media based on the change in polarization this media induces [75]. The obtained data must be fitted in order to get information about the complex index of refraction $\tilde{n} = n + ik$. Components of the refractive index for both materials at UV wavelengths are shown in Figure 3.2. As a substrate material, SiO_2 glass by Palik [76] was chosen from the

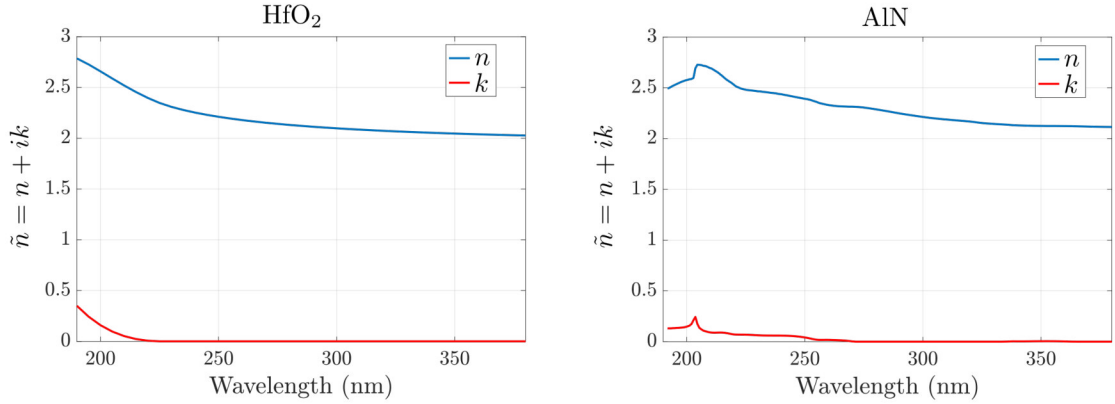

Fig. 3.2: Components of index of refraction $\tilde{n}$ for HfO_2 and AlN acquired as fits of ellipsometric measurements. The data were provided by Dr. Filip Ligmajer and Dr. Imrich Gablech for HfO_2 and AlN, respectively.

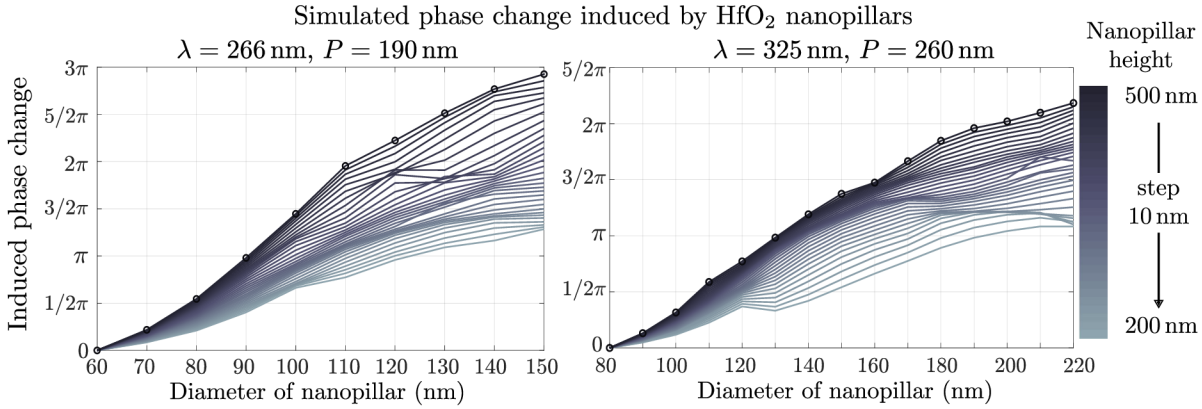

Fig. 3.3: Simulated phase change induced by HfO_2 nanopillars of a circular cross-section of varying diameters and height for two different incident wavelengths — 266 nm and 325 nm. The nanopillar is placed in periodic boundary conditions and the spacing between the adjacent nanostructures is kept constant at 190 nm and 260 nm for 266 nm and 325 nm wavelengths, respectively.

standard material library of the Lumerical software.

In this work, two different wavelengths of the plane wave illuminating the meta-atom were chosen — 266 nm and 325 nm. The wavelength of the incident light sets constraints on the spacing between the nanostructures P. In order to avoid diffraction effects induced by the array of the nanostructures, P must be smaller than the wavelength of the incident light. With this in mind, the spacing for the wavelength 266 nm was kept at $P_{266} = 190\,\text{nm}$ and for 325 nm at $P_{325} = 260\,\text{nm}$. The results of the simulations for HfO_2 and AlN can be seen in Figures 3.3 and 3.4, respectively. The height of the nanopillars varies from

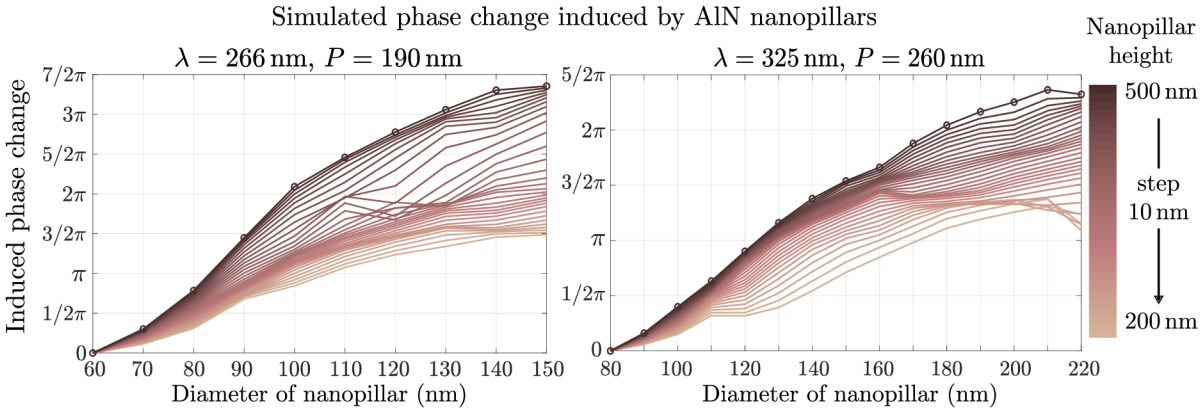

Fig. 3.4: Simulated phase change induced by AlN nanopillars of a circular cross-section of varying diameters and height for two different incident wavelengths — 266 nm and 325 nm. The nanopillar is placed in periodic boundary conditions and the spacing between the adjacent nanostructures is kept constant at 190 nm and 260 nm for 266 nm and 325 nm wavelengths, respectively. As can be seen, even in simulations for 266 nm wavelength, the induced phase change exceeds 3π which was not observed for the HfO_2 nanostructures of comparable height.

200 nm to 500 nm with 10 nm steps. The diameter of the nanopillar changes from 60 nm to 150 nm with 10 nm steps for the shorter wavelength 266 nm. For the longer wavelength, the minimum diameter of the nanopillar is 80 nm and goes up to 220 nm with 10 nm steps. The AlN nanopillars induce greater phase change than the HfO_2 to the incident light at both wavelengths and allow for phase manipulation, exceeding 3π for the light of 266 nm and nanostructures 420 nm and taller. This is due to the higher index of refraction of the AlN compared to the HfO_2 at 266 nm as can be seen in Figure 3.2. For both of the materials, taller structures are needed to cover the whole 2π phase range for the longer wavelength of the incident light 325 nm. This is intertwined with the phase induced by the propagation through the nanostructures — the longer the incident wavelength of light, the taller nanostructures are needed. In general, the AlN seems to be a better option because of its capability of greater phase manipulation, however, as it will be discussed in the following text related to fabrication, the fabrication precision needed for the 10 nm variation in diameter is problematic with AlN. The more viable option seems to be choosing taller nanopillars made out of HfO_2 due to the precision of fabrication.

In this work, the simulated nanostructures will be used to demonstrate the function of a metalens. In order to design a metalens, multiple steps must be taken. The phase profile of the metalens, as was written in the equation 1.3 in Section 1.1.2, gains a phase from 0 to multiples of π and one must know the wavelength of the incident light and the focal length of the final metalens. The phase profile is divided into steps, each covering only a phase from 0 to 2π, which is a sufficient range for a complete control of the light. Each phase step is then covered by multiple nanostructures of varying diameters (see Figure 3.5a), whose phase response to the incident light imitates the simplified phase

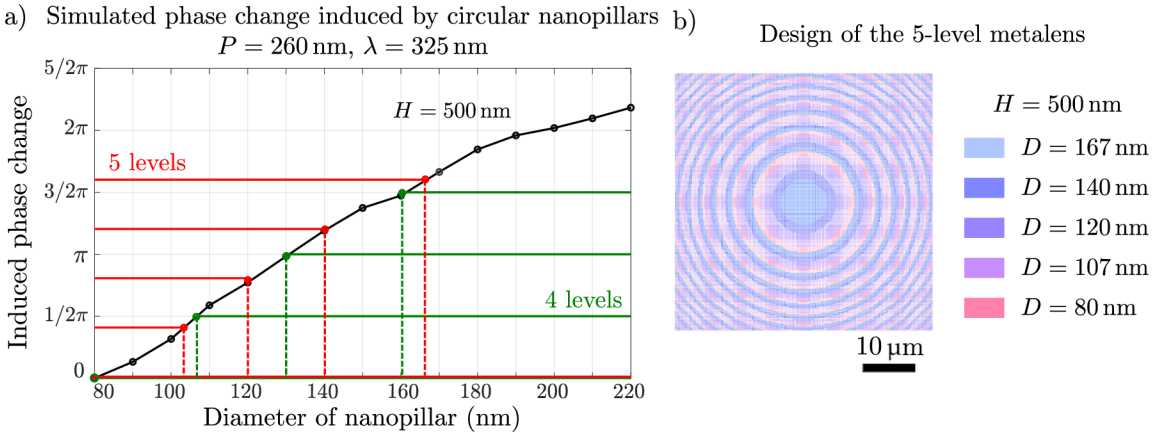

Fig. 3.5: Designing the metalens a) Choosing nanopillars of appropriate diameter for a given height of the nanopillar $H = 500$ nm for 4-level and 5-level metalens. b) Final design of the 5-level metalens composed of the previously selected nanopillars of varying diameter.

profile (see such profile in Figure 1.1 with Fresnel lens in Chapter 1). This leads to division of each step into multiple levels. In this work, 4 an 5 nanostructures covering each 2π step (and hence 4- and 5-levels) were used. The selection of the diameter of 500 nm tall HfO_2 nanostructures is demonstrated for a 4- and a 5-level metalens for the wavelength of 325 nm in Figure 3.5a. The final design of the 5-level metalens with a focal length $f = 150$ µm and numerical aperture NA = 0.3 is shown in Figure 3.5b. The functionality of such metalenses will be discussed in the following chapter related to the intensity profile measurements.

3.2 Electron beam lithography

Electron beam lithography (EBL) is a nanofabrication technique used for the very precise preparation of nanostructures by imprinting electron-exposed patterns into polymer layer. This technique employs accelerated electrons by tens of kilovolts whose de Broglie wavelength is then in order of Ångstroms and smaller [77, p. 86]. The high acceleration voltage shifts the diffraction limit significantly compared to light, which is used for a similar purpose in photolithography. The limitation of photolithography using visible light is improved if an extreme-UV source of light (e.g. 13.5 nm) is used. The preparation of the sample for EBL as well as the exposure by the electron beam will be discussed in the following text.

To perform electron beam lithography, an electron-sensitive polymer (called resist) is applied on top of the substrate via spin coating. During spin coating, the centrifugal force of the spinning ensures homogeneous spatial distribution of the applied resist. Every resist is marked with a specific number, for example, AR-P 6200.13, where the .13 suffix corresponds to the solid content percentage present in the resist, which is intertwined with the thickness of the final resist — the higher the solid content percentage, the thicker the resist for the same spin coating speed and acceleration. By adjusting the speed, acceleration and time of the spinning, as well as considering the viscosity of the resist, we can control the final thickness of the resist. After spin coating, the sample with the resist undergoes post-bake on a hot plate to ensure solidification of the resist. In order to imprint a pattern into the resist, energy transfer from the incident electrons to the atoms of resist must occur. This happens only in inelastic scattering events between the incident electrons and the electrons which surround the resist atoms during which the energy is deposited into the resist. Such scattering creates a chain reaction which leads to exposure of the resist [77, p. 89-90]. The dose of electrons D to which the resist is exposed can be written as:

$$D = \frac{I_\mathrm{b} \cdot t_\mathrm{d}}{d^2}, \tag{3.3}$$

where I_b is the electron beam current, t_d is the dwell time during which the beam stays in one place and d is the step size which corresponds to the smallest step that the beam takes during patterning of the desired design. Generally, we distinguish between two types of resist — positive and negative. In the positive resist, the polymer chains exposed to the electron beam are cut and then removed during the development of the resist. On the contrary, in the negative resist, the exposed chains of polymers become cross-linked and unlike the exposed ones remain on the sample after development [78, p. 344]. A schematic of the preparation process, exposure and development depending on the resist type is shown in Figure 3.6. It can be shown that the smaller the required pattern dimensions, the higher the beam energy (related to acceleration voltage) and the smaller the beam diameter must be [77, p. 86]. Apart from the energy of the electrons, high-resolution EBL requires a substrate of low mass density, reducing the backscattering of electrons which would increase the proximity effect, as well as rather thin resists, since electron scattering is more significant the deeper the electrons go into the resist. A resist mask with an imprinted design fabricated in this way can be further filled with a desired material or act as an etching mask to protect a material layer underneath the resist from etching.

One of the challenges present in EBL occurs already during the spin coating step. This is related to the adhesion of the resist to the used substrate. Generally, silicon has good adhesion to resists, however, for spin coating fuse silica, an adhesion promoter must be used. The adhesion promoter is applied before the resist and can be in a form of a liquid which is spin coated and soft baked, forming tens of nanometres thick layer. Another option is to use a gaseous adhesion promoter applied through vapour deposition, which is only a few nanometres thick or to use oxygen plasma treatment of the substrate before the resist spin coating. To ensure high precision of the patterning on non-conductive substrates, a conductive layer must be applied on top of the resist to prevent the sample charging, which would lead to unwanted electron beam deflection. The conductive layer can be in a form of a conductive poly-

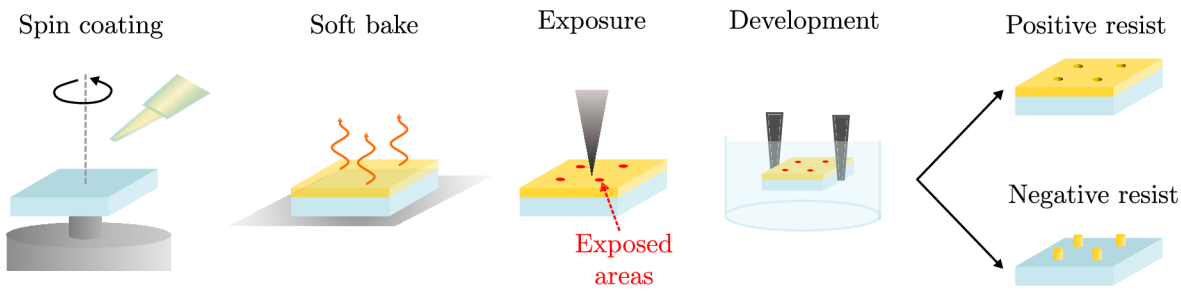

Fig. 3.6: Schematics of sample preparation and pattern imprinting via EBL into the positive and negative resist.

mer which is spin coated and soft baked on top of the resist or a metallic layer (a few nanometres thin). The conductive layer must be removed before the development of the resist, therefore it has to be done using chemicals which are not aggressive towards the resist. Another challenge present in EBL is the proximity effect, which is an indirect exposure of the resist by scattered electrons from the nearby. In general, the energy deposited into the resist is made up of two parts — a contribution from the direct exposure based on the desired design and an indirect contribution from the adjacent resist areas mediated by scattered electrons. The proximity effect enlarges the dimensions of the resulting structures in the design which can in the limiting case lead to blending together the designed structures. The last challenge worth mentioning is that if the sample with resist is heated up over a certain temperature referred to as a glass transition temperature, the resist can undergo a glass transition and can not be removed by a standard liquid solvent or even in oxygen plasma. The occurrence of the glass transition sets thermal constraints to the deposition technique which could be used for filling the EBL pattern to create the desired metasurface after the resist removal.

3.3 Deposition techniques

In nanofabrication, we distinguish between two main groups of deposition techniques — physical vapour deposition (PVD) and chemical vapour deposition (CVD) techniques. In PVD techniques, atoms of a solid target are vaporized in a vacuum towards the substrate on top of which the layer is grown. Examples of the PVD techniques include thermal evaporation, electron beam evaporation, magnetron sputtering, ion beam sputtering, pulsed laser deposition and more. The CVD techniques are based on chemical reactions of vaporized precursors, usually at high temperatures, which result in the growth of the desired material on top of the substrate. Atomic layer deposition is a good example of the CVD deposition techniques. Deposition by evaporation, sputtering and atomic layer deposition will be discussed in the following text, considering their general characteristics and advantages.

Deposition by evaporation is done via heating the desired material, usually in the form of pellets or powder placed in tungsten crucibles. The material in the crucible undergoes sublimation and creates vapour, which then rises from the crucible towards the substrate placed above and condenses on its surface. The heating of the material can be done either thermally via heating the crucible by an electric current or by the accelerated electron beam hitting the material in the crucible [79, p. 68]. Schematics of the electron beam evaporation, which uses accelerated electrons for evaporation of the material can be seen in Figure 3.7a: Formation of the electron beam is done via extraction

of electrons from a heated filament. The desired material in a crucible then presents an anode towards which the electrons are accelerated. For a certain electron current and acceleration voltage the target material starts to evaporate. Subsequent condensation on the substrate surface ensures the growth of the film from desired material.

Sputtering is another class of PVD techniques, in which is the material target sputtered off by accelerated ions. In this work, ion beam sputtering using a Kaufman-type source was the technique of choice. Ion beam sputtering uses accelerated electrons for the generation of argon ions. The argon ions are generated via inelastic scattering, where accelerated electrons eject the argon's electrons from the outermost shell, creating a positively charged argon ion. These argon ions are then extracted by an extraction grid towards a flat target made of the desired material which is kept at negative bias, accelerating ions to even higher energies. The momentum given by the positive ions to the atoms of the target causes them to sputter off and fly towards the substrate and deposit there. The just described process is schematically shown in Figure 3.7b. The main advantage of this deposition technique is the high energy of the sputtered atoms which enables their migration upon the substrate surface, allowing for good quality layers [80].

Atomic layer deposition (ALD) is a CVD technique and is based on sequential and self-limiting reactions of two gaseous precursors. The film is grown in cycles where only one precursor is present in the volume of the chamber and

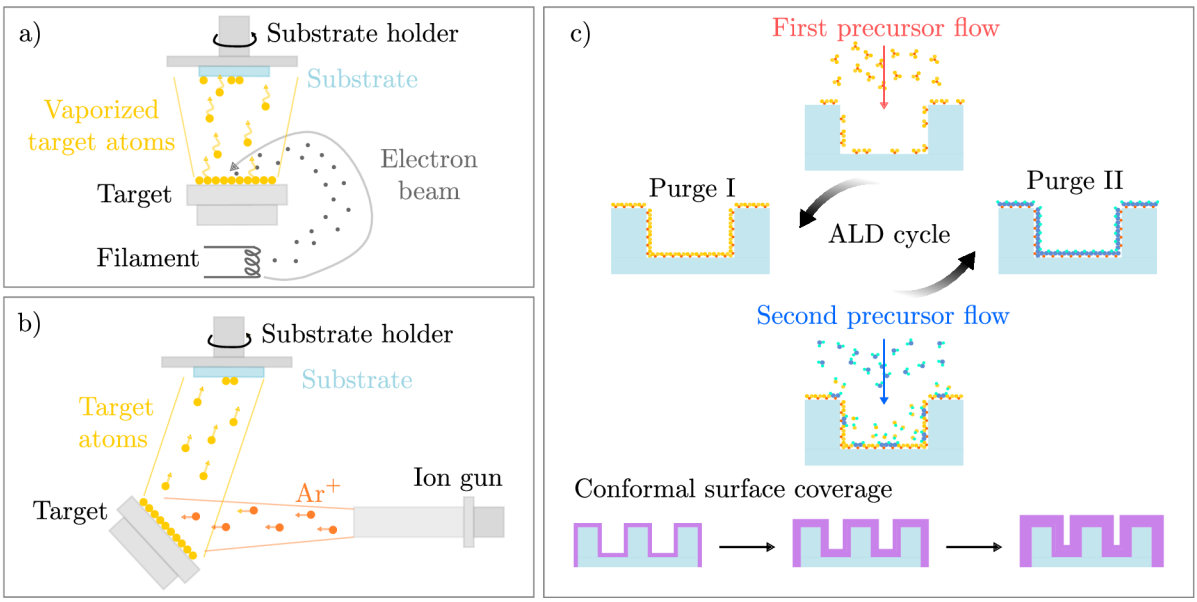

Fig. 3.7: Deposition techniques used for the fabrication of the samples in this work. a) Electron beam evaporation schematics. b) Ion beam sputtering schematics. c) Schematics of the cycle of ALD where precursors are kept separately in the chamber. This deposition ensures conformal coverage of the surface.

undergoes a self-limiting reaction with the substrate surface and with the other precursor. During the reaction of the precursors, not only the desired material on the surface is grown, but also volatile waste products of the reaction are present, as well as unused precursor molecules which must be purged from the chamber after each deposition cycle [81, p. 26]. This process is demonstrated in Figure 3.7c. The great advantage of this technique is that it ensures conformal deposition enabling coverage of substrates with complex topographies like nanostructured or porous ones. Another advantage of ALD is the capability to control the film thickness at an almost atomic level by changing the number of deposition cycles. The temperature of the deposition chamber in ALD is an important factor since it affects the growth rate [82]. If the temperature is too low, unwanted condensation of the precursor can occur. On the other hand, if the temperature is too high, molecules of precursors can decompose or even desorb from the surface. Both of these extremes cause uncontrolled growth. There is only the so-called "ALD process window" of acceptable temperatures where the reaction is still self-limiting and the growth rate can be controlled slightly by tuning the temperature [82].

The previous techniques can be compared based on the materials they can produce, the temperature used during the deposition or even the growth rate of the deposited material. Evaporation is usually used for the deposition of metallic materials, whereas ion beam sputtering is used for more complex metallic compounds such as nitrides. During the nitride deposition, a second source of nitrogen ions is used — this is so-called dual-beam ion sputtering. ALD is often times used for the deposition of oxides or nitrides as well. Considering the temperature, both evaporation and ion beam sputtering can take place at room temperature. However, during sputtering, the sample gets heated by the impinging high-energy ions which may unintentionally heat the sample. As was stated before, ALD has a limited window of temperature where the growth is controlled. To ALD recipes taking place at 90 °C, we will refer to as low-temperature ones. These deposition techniques could be compared based on the growth rates, which depend on many parameters. The ALD is the slowest technique out of the mentioned ones and therefore, it is used mainly for the fabrication of ultra-thin and thin layers (units to higher tens of nanometres). This, however, can be employed well in the fabrication of high aspect-ratio nanostructures by deposition into thick resists with features of small lateral dimensions, where the thickness of the desired layer must be only half the largest diameter of the design thanks to the conformal coverage ALD provides, as schematically depicted in Figure 3.7c.

3.4 Etching techniques

When speaking of etching techniques, we distinguish between two main groups — wet and dry etching techniques. In wet etching techniques, the etchant is a chemical solution and the etching direction is usually isotropic, meaning that the etching occurs in all directions with equal rate [77, p. 234]. Due to the etching isotropy, wet etching is advantageous to use when cleaning wafers or when removing metallic cappings which were deposited in the previous fabrication steps. Achieving anisotropy in wet etching is possible only for specific crystalline materials like silicon, for example [77, p. 236]. Introducing the etching anisotropy is easier in dry etching techniques employing gases as etchants. The etching direction can be tuned by optimizing the flow rates of reactive gasses in reactive ion etching (RIE) or the angle of incidence in an ion beam etching. For the fabrication of high aspect-ratio nanostructures with smooth sidewall profiles, anisotropic etching is crucial. Therefore, only dry etching techniques will be further discussed.

Ion beam etching usually employs argon ions which are generated in a very similar nature as during the deposition by ion beam sputtering. That is by a collision of accelerated electrons with argon gas. However, in this case, the ion gun producing the ions is targeted towards the sample surface. This technique is based purely on physical etching in which the momentum is transferred from the incident argon ions to the atoms of the sample, which are then sputtered away as is schematically shown in Figure 3.8a. During this process, the sample can be tilted to change the angle of the incident ions and therefore the main direction of etching, and also rotated to ensure a uniform etch rate over the sample surface.

In RIE, the dominant phenomenon is not physical but rather chemical etching caused by chemical reactions between reactive gasses such as fluorine, chlorine, bromine or iodine [77, p. 240]. These gasses are used for their high reactivity, allowing for the etching of many inorganic materials. The ionization of these reactive gasses is done again by the interaction of gas atoms with accelerated electrons, where the former lose electrons of the outermost shell. During the etching, ions of previously mentioned elements react with the surface atoms of

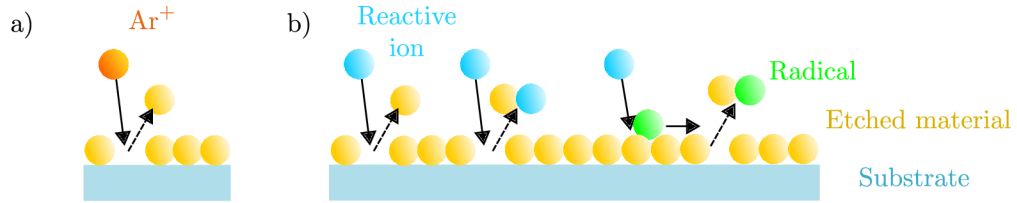

Fig. 3.8: Schematics of etching mechanisms in: a) Ion beam etching b) RIE.

the sample, forming a volatile compound that is purged out of the chamber to prevent redeposition. During RIE, four various processes depicted schematically in Figure 3.8b take place. Aside from the already mentioned volatile compound formation, there is a physical sputtering by the incident ions, which is similar to ion beam etching done by argon ions. There are another two mechanisms intertwined by the generation of radicals on top of the sample. This happens via the dissociation of adsorbed gas molecules by the incident ions and the consequent reaction of radicals with atoms of the sample, which then form volatile compounds. There are multiple ways to etch one material using different combinations of reactive gases as can be seen in Table 3.1, which presents a few examples related to the topic of this thesis. The type of the reactive gases, their flow and the ratio of the flow can affect the anisotropy as well as the rate of the etching. Optimization of the RIE recipe is crucial for obtaining precise and directional etching profiles.

Considering the previous chapter related to metasurfaces for UV wavelengths, a precise fabrication process is often behind their impressive performance. One way of the fabrication utilizes EBL in the first step, which is followed by a low-temperature deposition of the desired material, subsequent etching takes place, and then the EBL resist is removed in the final step. During the first step, the electron-exposed areas of the positive resist become holes that can be consequently filled by the desired material. The second step is the deposition of material into the formed holes, where the only limitation is the deposition temperature since most of the polymethyl methacrylate (PMMA) resists can not withstand more than approximately 105 °C [87]. Deposition temperatures lower than 100 °C ensure that the resist does not undergo glass transition and can be removed from the sample in the final step. For thin oxide layers, low-temperature ALD is the technique of choice. Since this technique allows for the conformal coverage of the surface and hence forming high aspect-ratio nanostructures does not require precise wet or dry etching techniques during the fabrication process. In order to remove the resist after the deposition, the deposited material on top of the resist must be etched away. This is usually done by utilizing one of the dry etching techniques such as reac-

Tab. 3.1: Possible etching gases or gas mixtures of materials used during fabrication in this work with references (Ref.).

Material	Etching gases	Ref.
AlN	Cl_2, BCl_3, SF_6, O_2, Ar combinations	[83]
HfO_2	Cl_2, BCl_3, SF_6, Ar combinations	[84]
Cr	O_2, CCl_4, CO_2, Ar combinations	[85, 86]
Resist	O_2	[87]

tive ion etching or ion beam etching, considering the requirement of precision in terms of the directionality is not tight since it only affects the final height of the designed nanostructures. High aspect-ratio nanostructures suitable for UV applications, which were fabricated via the previously mentioned process, employing HfO_2 and Nb_2O_5 nanopillars are shown in the scanning electron microscope (SEM) images in Figure 3.9. This approach will be demonstrated in the following section related to fabrication optimization of HfO_2 nanostructures. For materials, for which low-temperature deposition is not an option, a different approach, utilizing carefully optimized directional etching over a mask, must be chosen. This fabrication approach starts with the deposition of the desired material first and then subsequent resist patterning via EBL and etching through a hard- or resist-mask. The need for precise and well-optimized etching is crucial for this approach. Both of these approaches were demonstrated in the fabrication of TiO_2 nanostructures for visible wavelengths [29, 30]. For UV wavelengths, however, the nanostructures reach even smaller sizes while keeping their high-aspect-ratio nature, which makes the fabrication more challenging compared to the metasurfaces for visible wavelengths.

As was shown in the previous sections 2.3, 2.4, many results reported so far in literature are proposals of theoretical designs and simulations, leaving us only with a few really functional and experimentally verified samples that employ ALD as the deposition technique. Due to this, it was possible to achieve high quality of the fabricated thin films, with the desired fabrication precision implanted by the previous EBL fabrication procedure. In this work, the aim is to fabricate nanostructures from HfO_2 or AlN and demonstrate their potential on the functional sample. The next sections will be regarded to the optimization of fabrication of HfO_2 metalens, which employs ALD into a previously patterned resist mask by EBL. The optimization of fabrication of AlN nanostructures can be found in Appendix A, which unfortunately did not

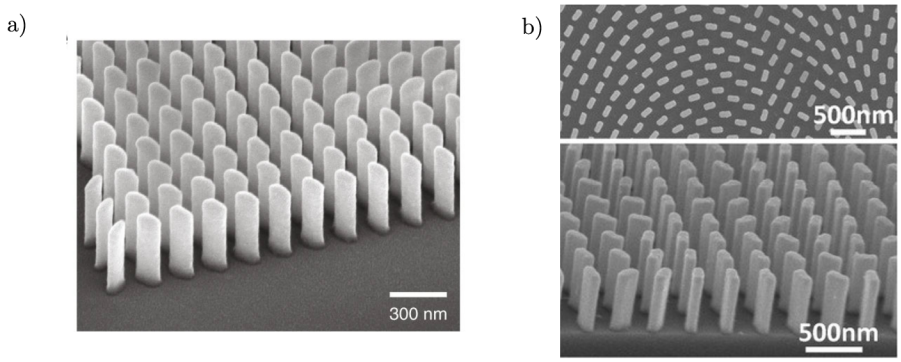

Fig. 3.9: SEM images of a) HfO_2 and b) Nb_2O_5 nanopillars of elliptical and rectangular cross-section respectively, fabricated via ALD into positive resist mask. Adapted from [47, 49].

lead to demonstration of functional sample due to the insufficient precision in fabrication of the nanostructures.

3.5 HfO_2 metasurface fabrication

The fabrication of HfO_2 metasurface consists of multiple steps which are schematically shown in Figure 3.10, and which were in principle discussed in previous sections. This fabrication approach employs the EBL into a positive resist, forming holes, which are consequently filled with the desired material. As discussed in the previous Section 2.4, approach employing deposition into a resist mask yielded the most promising results considering functional samples. The following describes optimization steps taken towards the fabrication of the final HfO_2 metalenses.

In this work, the fabrication optimization was done for two different wavelengths of the incident light — 266 nm and 325 nm, which affects the spacing between the nanostructures as well as their height. The spin coating and EBL were tested on designs suitable for the 266 nm wavelength of the incident light — the height requirement set by numerical simulations discussed in the next chapter for such nanostructures was around 350 nm. However, the nanostructures had to reach much greater precision in the lateral size with spacing only 190 nm, which was set in order to avoid diffraction effects of the array. As a substrate, 300 µm thick fused silica was used due to its low absorption of UV light, as was discussed in Section 2.1. The whole fabrication process starts with the spin coating and subsequent soft bake of the resist. As was discussed in Section 3.2, the adhesion of the resist to fused silica substrate is poor. Therefore, tests were done for both liquid adhesion promoter from the

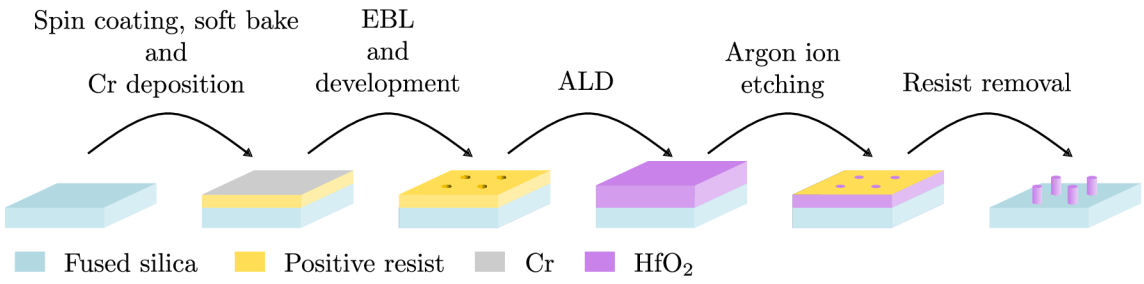

Fig. 3.10: Schematics of HfO_2 metasurface fabrication. First, the sample is prepared for EBL via spin coating of positive resist and deposition of conductive Cr layer. The prepared resist is patterned by EBL based on the design and the holes formed in the resist after development are filled with the HfO_2 by ALD. Due to the conformal coverage provided by ALD, the top layer of HfO_2 must be etched down to the resist surface, which can be consequently removed in oxygen plasma.

Allresist Company AR 300-80 ([88]), which is applied through spin coating and subsequent soft bake, and for hexamethyldisilazane (HMDS), which is the gaseous adhesion promoter applied through evaporation, while the sample is placed between two hot plates at the temperature of 135 °C [88]. The application parameters of adhesion promoters are summarized in Table 3.2a. The estimated thickness given by the product information is 15 nm for the AR 300-80, whereas only around 5 nm for the HMDS [88]. The adhesion promoters were compared, using positive resist AR-P 6200.13 and the results can be seen in Figure 3.11: Images from the scanning electron microscope (SEM) showing the HfO_2 nanostructures fabricated using liquids (AR 300-80) and gaseous (HMDS) adhesion promoter. For fabricating tall nanostructures, it is more favourable to use the gaseous promoter HMDS instead of the liquid promoter AR 300-80. Falling of the nanostructures is still reoccurring on the edges of the patterned fields, which is due to the proximity effect. The edge nanostructures miss the neighbours from one of their sides, which results in lower and possibly insufficient dose. In terms of the resists, three different positive resists AR-P 6200.13 [89], AR-P 669.04 [87] and AR-P 617.08 [90] from the Allresist company were tested as can be seen in Table 3.2b. For the nanostructures suitable for the wavelength 266 nm, a resist of only around 430 nm is sufficient

Tab. 3.2: Summary of products used during preparation of the samples for the EBL tests. a) Table of adhesion promoters tested by EBL into the AR-P 6200.13 resist of 430 nm thickness and parameters used for their application. b) Table of tested positive resists on top of HMDS adhesion promoter, spin coating speeds/accelerations, parameters of consequent soft bake and measured thickness by s reflectometer. c) Table of conductive layers tested during the fabrication optimization and their application parameters.

a) Adhesion promoters

Product	Application parameters	Product info
AR 300-80	4000 rpm/ 2000 rpms/ 60 s and soft bake 180 °C for 120 s	[88]
HMDS	135 °C for 2 minutes hot plate evaporation	[88]

b) Spin coating parameters for different resists on HMDS base

Product	Spincoating (for 60 s)	Soft bake	Thickness (nm)	Product info
AR-P 6200.13	4000 rpm/ 2000 rpms	150 °C/ 60 s	430	[89]
AR-P 669.04	1800 rpm/ 2000 rpms	150 °C/ 180 s	427	[87]
AR-P 617.08	4600 rpm/ 3000 rpms	200 °C/ 300 s	520	[90]

c) Conductive layers

Product	Application parameters	Product info
AR-PC 5090.02	2000 rpm/ 500 rpms/ 60 s and soft bake 150 °C/ 60 s	[91]
Cr	electron beam evaporation	–

for the fabrication. The thickness of the resist was measured on a silicon substrate by a reflectometer Ocean Optics NanoCalc 2000. The parameters needed to obtain sufficiently thick layers and the measured thicknesses are shown in Table 3.2b. To prevent the sample from charging during the EBL, 10 nm of chromium was deposited in BESTEC electron beam evaporator. There is also a polymerous conductive layer available of AR-PC 5090.02 applied through spin coating [91], however, the layer is tens of nanometres thick and highly non-uniform on the resist surface which manifests into the comet-like shapes not suitable for further use in fabrication. Sample prepared in this way can then undergo imprinting the pattern by EBL.

The design for the EBL were $(20 \times 20)\,\mu m^2$ arrays composed of nanostructures of varying diameter within each array, as can be seen in Figure 3.12a. The dose range selected for each resist is listed in Table 3.3a with a coarse step of $10\,\mu C/cm^2$ between the doses. The EBL was performed on Raith 150 Two, which is a high-resolution low-voltage lithography system. The dose tests were carried out with the 20 kV acceleration voltage, which is optimal for the instrument due to the presence of beam booster, which improves the performance and stability of the lithographic instrument. The 15 µm aperture (corresponding to beam current around 65 µC) and write filed size of $(40 \times 40)\,\mu m^2$ were set for patterning this design. Before developing the resists, the Cr layer was etched down by wet etching for 10 s in TechniEtch Cr01 (Microchemicals [92]). The development parameters based on the used resist are shown in Table 3.3b. The results of the performed EBL, already filled with the HfO_2, can be seen in Figure 3.12b: The AR-P 6200.13 performs very well, considering both the adhesion of the nanostructures to the substrate as well as the fabrication of nanostructures with the smallest lateral dimension compared to the other resists. The worst result in terms of lateral resolution and height was yielded by

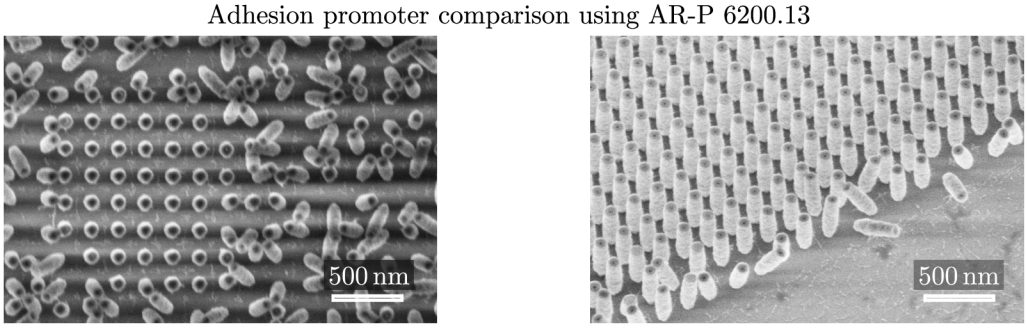

Fig. 3.11: The comparison of adhesion of the nanostructures fabricated by EBL into the AR-P 6200.13 of 430 nm thickness when using AR 300-80 and HMDS as the adhesion promoters. The adhesion of the nanostructures when using HMDS was much better with nanostructures fallen-down only at the edges of the patterned fields.

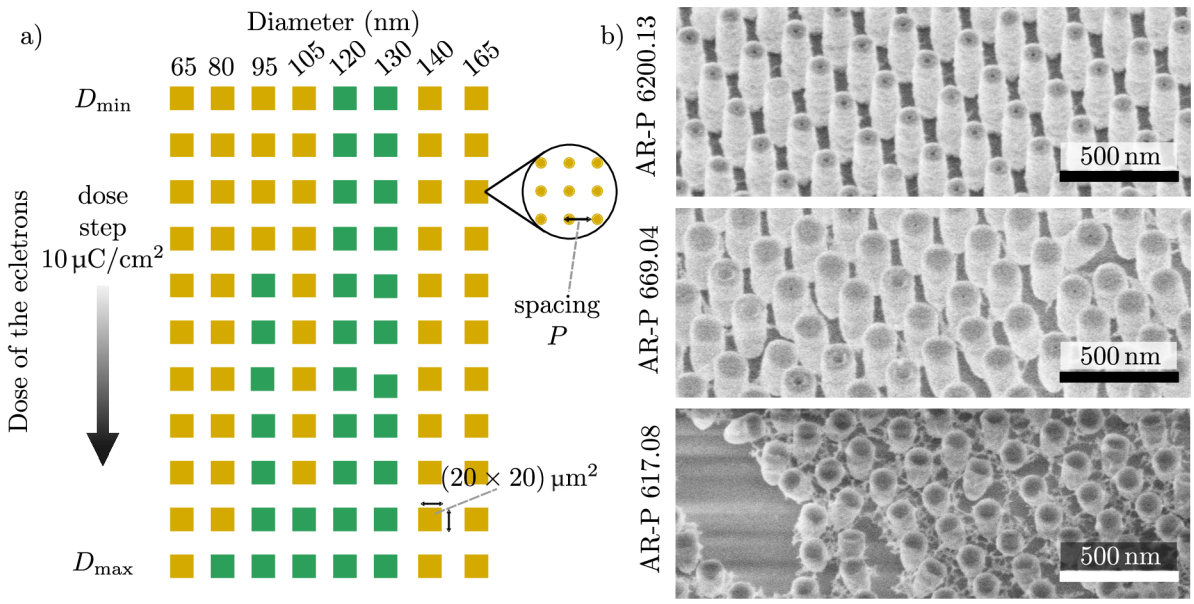

Fig. 3.12: a) The design used for the tests of multiple positive resists. An array of nanostructures with the diameter of the nanostructures in each field. The dose test was carried out based on the doses written in Table 3.3. The spacing between the nanostructures was kept constant at $P = 190\,\text{nm}$ and the field size was $(20 \times 20)\,\mu\text{m}^2$. The green squares mark the nanostructures which did not fall down during the fabrication. b) SEM images of the nanostructures in 35° tilt fabricated using resists according to Table 3.3. Both the lateral resolution as well as the adhesion of the nanostructures is the most promising for the AR-P 6200.13, hence, only this resist was used for the fabrication of the functional metasurface.

Tab. 3.3: Parameters related to set doses during the EBL patterning and development procedures based on the used resist. a) Table of tested doses of structures in arrays with constant spacing $P = 190\,\text{nm}$ and array size $(20 \times 20)\,\mu\text{m}^2$. The doses varied from the minimum dose D_{min} to the maximum dose D_{max} with a coarse dose step $10\,\mu\text{C/cm}^2$. b) Chemicals and times used for the development based on the type of resist.

a) Doses

Resist	D_{min} (µC/cm²)	D_{max} (µC/cm²)
AR-P 6200.13	60	210
AR-P 669.04	200	410
AR-P 617.08	60	210

b) Development parameters

Resist	Developer chemical and time
AR-P 6200.13	AR 600-546/ 60 s and isopropyl alcohol/ 30 s
AR-P 669.04	AR 600-56/ 90 s and isopropyl alcohol/ 30 s
AR-P 617.08	Methyl isobutyl ketone/ 60 s and isopropyl alcohol/ 30 s

the 617.04, which also shown the visible tears within the arrays. This resist was tested mainly for its high glass transition temperature of 150 °C, which

would allow for higher temperature depositions. Based on these results the resist AR-P 6200.13 was used for further fabrication.

The holes of the patterned resist in the EBL step were consequently filled by the atomic layer deposition (ALD) of the HfO_2 by CambridgeNanoTech Fiji 200. This deposition is thermal, meaning that the besides inorganic precursor tetrakis(dimethylamino)hafnium (TDMAH), the second precursor is water. This deposition takes place at 90 °C to prevent the resist from undergoing the glass transition, the TDMAH precursor must be heated to 78 °C to ensure the evaporation of the precursor, which can be then flown into the chamber. The inlet end purge of the precursors is provided by the carrier and purge gas, which is argon and is set to 60 sccm and 200 sccm for the carrier and purge gas, respectively. As the first step, the water precursor is flown into the chamber with the pulse duration being 0.06 s and purge time being 30 s. Then the TDMAH is flown in the chamber where the 0.25 s and 30 s are the pulse and purge time, respectively. The thickness of the grown HfO_2 was estimated as 1.4 Å/cycle from a fit of the ellipsometric measurement done by Dr. Filip Ligmajer. The conformal coverage provided by the ALD is of great importance in the fabrication process since the layer thickness does not need to correspond to the height of the nanostructures but only to the radius of the biggest nanostructure in the design. To ensure the proper fill of the nanostructures, about 200 more cycles than needed are performed during the deposition. On the other hand, the conformal coverage prevents the possibility to remove the resist directly after the deposition as in standard lift-off processes, where the material is deposited on top of the resist and the resist edges are still accessible to the resist remover. Therefore, the argon ion etching was employed in the next step.

The argon ion etching took place at the Scia Systems Coat 200. During the etching, the backside cooling of the holder was ensured indirectly by helium flow set to 10 sccm during the etching. The sample was tilted to 60 ° and rotated by 10 rpm (revolutions per minute), providing better uniformity and lowering the possibility of redeposition during the etching. Various parameters can be set at the instrument, the most important are the powers, voltages and currents of the ion beam source and ion beam neutralizer. The instrument uses a microwave ion beam source with the power set to 300 W while both beam and acceleration voltage were set to 400 V. The neutralizer uses a radio-frequency power source set to 55 W with the cathode being kept at 48 V, the current set to 800 mA, and the keeper power to 30 W. The measured current of the ions was 0.075 mA/cm^2. The etching time varies based on the thickness of the deposited dielectric material by the ALD. Fortunately, the instrument has also a mass spectrometer, so one can monitor the decrease of the material while etching. It is convenient to etch approximately 90 s more after the mass

spectrometer monitor values drop to the minimum, to ensure complete removal of the material. The sample with the sputtered-off top layer is ready for the removal of resist in oxygen plasma in the resist stripper Diener electronic NANO Plasma cleaner, where the plasma is ignited by a combination of flows of oxygen and argon, while the main etch phase takes place with 20 sccm oxygen only. The 60 min duration of this process was sufficient for full removal of the 430 nm thick resist, however, for thicker resist, the duration must be extended.

Generally, when performing the dose tests, one tries to find the optimum doses so the designed nanostructure size is the same as the resulting nanostructure patterned by EBL. After performing three different dose tests for the AR-P 6200.13 resist (two for the adhesion promoters and one for the resist comparison), a different approach was chosen. The most promising results in terms of the robustness of the fabricated nanostructures were shown for only four nanostructure diameters in design — 80 nm, 95 nm, 120 nm and 130 nm, as can be seen in Figure 3.12a, where the green squares mark the nanostructures which did not fall down during the fabrication. Based on the dose of electrons given to these nanostructures, the diameters of the final nanostructures vary — the bigger the dose, the bigger the diameter of the resulting nanostructure, which allows for covering wide range of different sizes of nanostructures. This fabrication approach based on the variation of the electron dose was employed mainly because the results were repeatable in terms of the final nanostructure size and also its adhesion to the substrate.

In order to characterize the optical response of the fabricated nanostructures, a light source of 266 nm was needed. Unfortunately, due to the unavailability of such source at the time, another fabrication round for the incident light of 325 nm took place. As the longer wavelength of the incident light was chosen, the minimal height of the nanostructures changed to ca. 450 nm, as well as the spacing increased to 260 nm. Based on these changes, the fabrication process must have been altered as well. First alteration was in the spin coating, where the parameters of the AR-P 6200.13 were adjusted to speed 3000 rpm, acceleration 2000 rpms and time 60 s, which led to the final resist thickness of 550 nm. The soft bake of the resist was prolonged to 90 s due to its increased thickness. The dose test designs then employed only two sizes of circles with diameters 95 nm and 120 nm, which acquired the desired size due to the choice of appropriate electron dose. The doses in this dose test varied from 145 $\mu C/cm^2$ to 230 $\mu C/cm^2$ with a finer 5 $\mu C/cm^2$ step for both 95 nm and 120 nm structures. The size in the design, appropriate dose and measured size of the final nanostructures for spacing $P = 260$ nm and height $H = 500$ nm can be seen in Table 3.4, which summarizes the nanostructures needed for fabrication of 4- and 5- level metalens whose functionality will be discussed in the next chapter. The target size corresponds to the size of the ideal nanostructures

Tab. 3.4: Optimal electron doses given to the nanostructures of 95 nm and 120 nm in diameter with constant spacing $P = 260$ nm and height $H = 500$ nm to achieve various nanostructure sizes after the resist development, which are suitable for the a) 4-level metalens b) 5-level metalens. The estimated size refers to the optimal size based on the simulations as mentioned in Section 3.1, the real size is the measured size based on the carried-out dose test.

a) 4 level metalens

Target size (nm)	Size in the design (nm)	Dose (µC/cm^2)	Real size (nm)
80	95	150	83
108	95	175	108
130	95	200	130
	120	165	129
160	120	195	159

b) 5 level metalens

Target size (nm)	Size in the design (nm)	Dose (µC/cm^2)	Real size (nm)
80	95	150	83
104	95	170	104
120	95	190	129
	120	150	121
140	95	220	141
	120	175	144
167	120	205	167

proposed by the simulations, whereas the real size corresponds to the measured size of the nanostructures after fabrication. For some of the target sizes both nanostructures 95 nm and 120 nm in diameter can be used with varying doses, yielding structures of comparable real size. Due to the increase of the resist thickness, the effect of the acceleration voltage during EBL was tested. Figure 3.13 shows nanostructures of the same design size exposed to the same electron

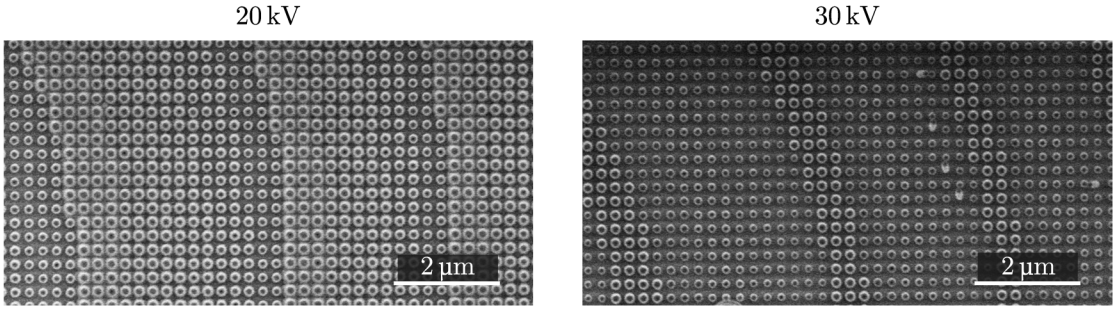

Fig. 3.13: Comparison of the acceleration voltages used during EBL on the Raith 150 Two. Even though the instrument is more stable at 20 kV, the 30 kV acceleration voltage yields much better result mainly due to the lower proximity effect, which results in better lateral resolution and well-defined and separated nanostructures. Because of this, the 30 kV acceleration voltage was used for the fabrication of the final metalens.

dose, yet with varying acceleration voltage. The 30 kV provide much better results than 20 kV due to the higher penetration depth of the electrons into the resist. The nanostructures fabricated with 30 kV acceleration voltage have also much better spatial resolution and well-defined spatial separation between them too. The ALD recipe as well as the subsequent ion beam etching were the same as for the nanostructures targeted at 266 nm wavelength. The resist was removed in the oxygen plasma as in the previous fabrication, however, the removal time of 120 min was necessary to remove the resist fully. SEM images of the final metalens as well as a close-up of the nanostructures are shown in Figure 3.14a,b. In Figure 3.14c it can be seen that the nanostructures truly have a high aspect ratio between the diameter and the height (ca. 5). The height of the nanostructures based on the SEM images was measured to be (500 ± 10) nm.

During the fabrication, multiple complications came up: The first one was the development of cracks in the resist of thickness 550 nm during the fabrication process. The cracks in the resist lead to etching of the substrate during the ion beam, which can be seen in Figure 3.15a. The resist cracks form during the ALD deposition when the sample is heated to 90 °C for approximately 17 hours. The cracks are most likely caused by insufficient adhesion of resist to the substrate at some places or water residues on the substrate caused by the previous substrate cleaning. This can be avoided by baking out the substrate for tens of minutes after cleaning and also using oxygen plasma cleaning right before spin coating. Fortunately, these cracks are rarely present within the patterned areas since the resist is not present there after the development.

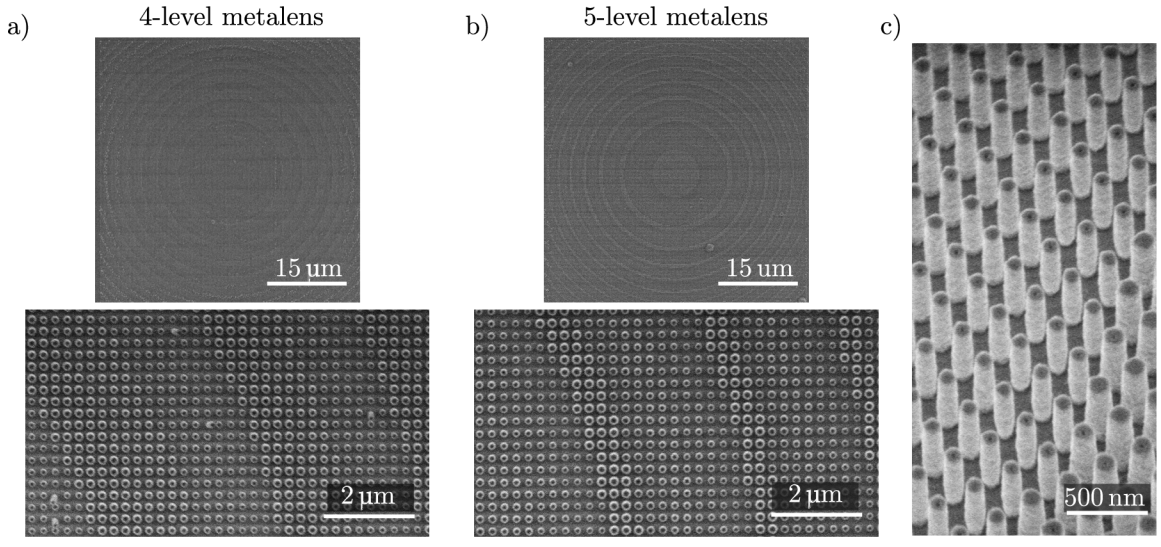

Fig. 3.14: SEM images of the final 4- and 5-level metalenses. a) 4-level metalens from the top view and close up. b) 5-level metalens from the top view and close-up. c) Nanostructures forming the final metalenses in 35° tilt, height was measured from the SEM images and was estimated to be (500 ± 10) nm.

The second complication was the occurrence of hollow nanostructures. The nanostructures seen in Figure 3.15b were deposited with the same parameters as the ones in Figure 3.14, however, as can be seen, the holes are much more apparent in the former. The problem might be that the water pulse in the ALD recipe was too short or solely in the change of the conditions inside the chamber caused by previous depositions. The occurrence of such artefact will not be further optimized in this work, however, due to its significant effect on the performance of the metalens, it will be discussed in the next chapter related to metalens measurements. Finally, the greatest problem of the metalens fabrication is the strong proximity effect. The design of the metalens is composed of many concentric circles of nanostructures. Within every few concentric circles, the structure diameter rises from the smallest to the biggest diameter and then is followed by the nanostructure of the smallest diameter again, forming the 2π steps in the design. The dose tests were carried out on arrays of nanostructures with the same diameter within each array and, therefore, the doses in the metalens design and in the tested arrays do not match exactly. The nanostructures in the metalens thus often happen to be bigger

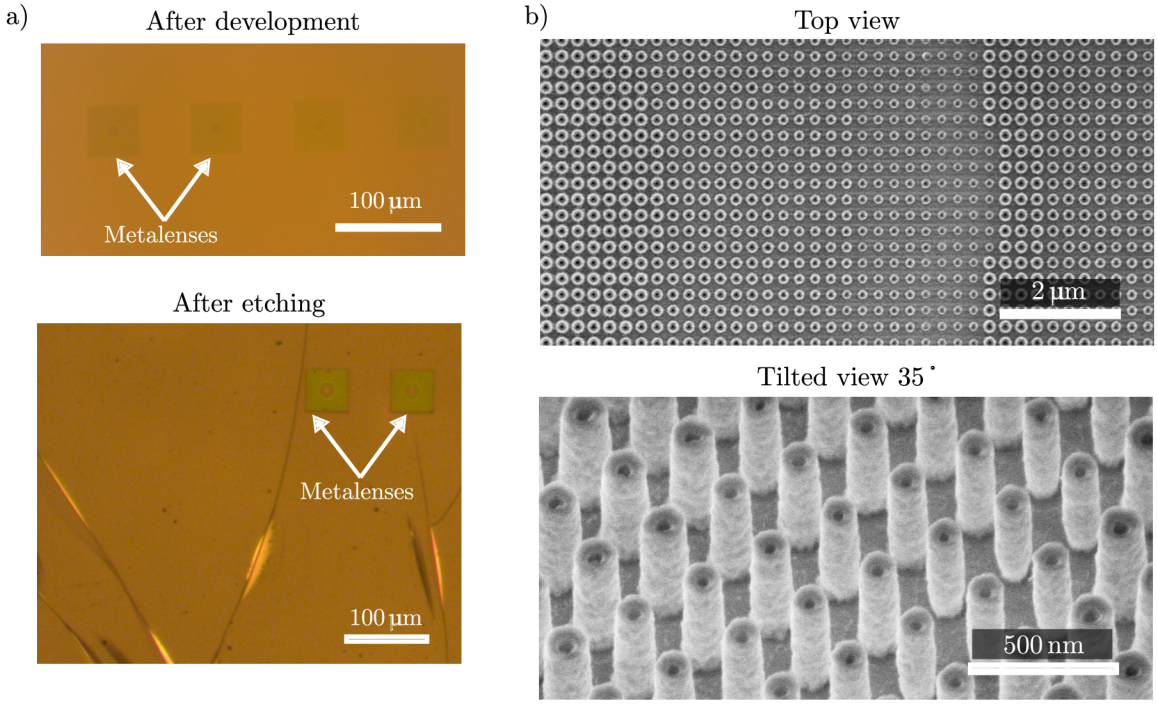

Fig. 3.15: Complications during the metalens fabrication. a) Optical microscopy images of cracks in the resist formed during the ALD deposition. The upper image is after the development and before the deposition, the bottom image is after the ion beam etching and resist removal. The cracks in the resist resulted in etching of the substrate beneath it. b) SEM images of hollow nanostructures formed even for sufficiently long deposition with unchanged parameters compared to the nanostructures in 3.14.

than the target size. This problem can be solved by a thorough proximity correction, which is planned for future fabrication rounds.

To conclude this chapter, the optimization of HfO_2 nanostructures was thoroughly described, leading to the successful fabrication of metalens as a functional sample. Obstacles such as cracks of the resist, hollow nanostructures and the proximity effect were discussed with the possible solutions. Besides HfO_2, AlN was proposed as suitable material as well, however, the fabrication optimization did not lead to applicable results in terms of functional metasurface and is thoroughly described in Appendix A. Measurements of the metalens from HfO_2 will be discussed in the next chapter.

3.6 Custom optical setup

In order to optically characterize the fabricated metasurfaces, a custom optical setup was built, which uses a He-Cd laser of 325 nm wavelength and 15 mW power (Kimmon Koha model IK5551R-F [93]) for evaluation of the functionality of the fabricated metalenses. This setup allows for imaging along the z-axis of the sample and measuring the intensity at a given distance from the sample surface. Such measurements can evaluate the focusing efficiency of metalenses. It is crucial to use optical components suitable for UV light otherwise large part of the light gets absorbed before it reaches the sample surface. Aluminium mirrors as well as an objective lens suitable for near-UV wavelengths with working distance WD = 0.8 mm and numerical aperture 0.47 and magnification 40 (Thorlabs LMU-40X-NUV [94]) was used in the setup which is shown in Figure 3.16. As can be seen there, the UV light goes via multiple reflections on aluminium mirrors through the metasurface which alters the light path. The wavefronts behind a metasurface then then propagate through the objective and a tube lens and finally impinge on the spectrograph camera through the aperture, which allows for spatial selection on the sample surface such that only one metalens is measured. The field of view of the spectrograph's camera is very small (ca. 300 µm) and therefore inconvenient for navigation on the sample surface. Because of that, another branch with a camera employing white light illuminates the sample through the beam splitter and the objective lens for the orientation on the sample. The spectrograph used was Andor Kymera 193I (model 193I-B2-SIL [95]) with the Newton 971 EMCCD camera (model DU971P-BV [96]). The camera quantum efficiency for 325 nm is only around 10% at a room temperature (given by the information of the manufacturer), however, with the availability of the electron multiplier and cooling, the signal was sufficiently high for measurements.

In this chapter, the main tools used for design, fabrication and measurements of the functional samples were discussed. The whole process started

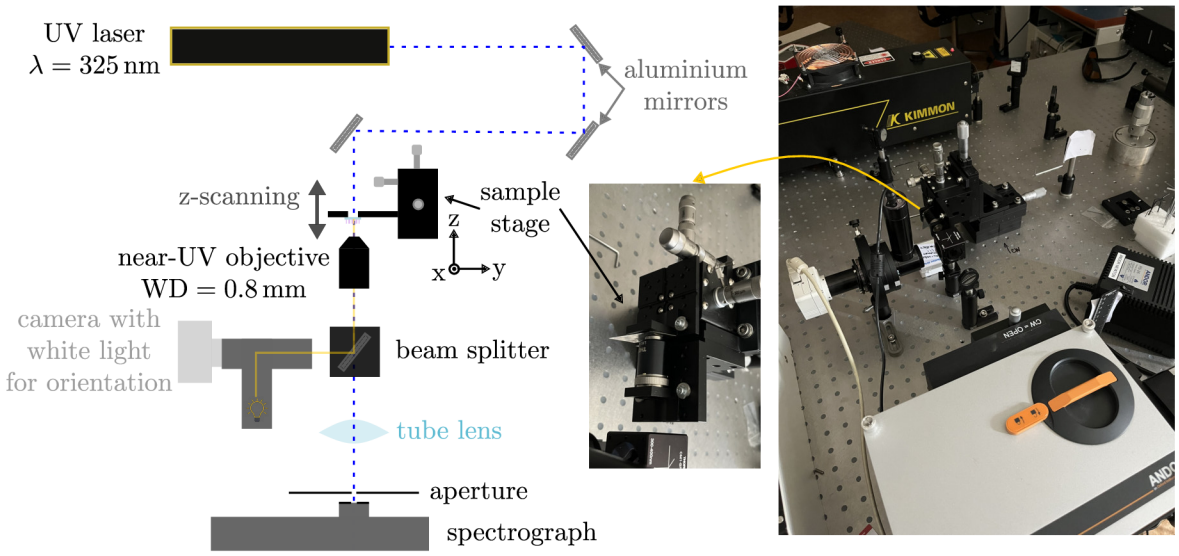

Fig. 3.16: The experimental optical setup used for the sample characterization, allowing for z-scans of the intensity of the UV light which propagated through the sample. Measurements done using this setup demonstrate the focusing capabilities of the final metalens. Left-hand side — schematics, right-hand side – a photograph of the real optical setup with a close-up of the sample stage. Distance between the holes of the optical table is 2.5 cm for a scale in the optical setup photograph.

with numerical simulations crucial for the estimation of the optical response of the nanostructures. Then, by employing multiple fabrication methods, such as EBL, electron beam evaporation, AlD, RIE and ion beam etching, the fabrication optimization of HfO_2 nanostructures was discussed. The chapter was closed with the description of the custom optical setup. This setup was used for characterization of the final HfO_2 metalens, which will be described in the next chapter.

4 Results

In this chapter, the functionality of the fabricated 5-level metalenses, thoroughly described in Section 3.5, will be discussed. To verify that the meta-atoms forming the final metalens induce the same phase as the simulations discussed in the previous chapter suggest, measurements of the induced phase are needed. Such measurement can be done in a holographic optical setup, where the incident light is split into two branches, a reference one with only the empty substrate, and another one with an array of meta-atoms. After passing through the array, the light from both branches interferes and forms an interference pattern, from which one is able to calculate the phase induced by the meta-atoms. However, due to unavailability of a powerful-enough source of UV light of either 266 nm or 325 nm, this measurement was not carried out. Instead, intensity profiles behind the final metalens with designed focal length $f = 150\,\mu\text{m}$ were measured in the optical setup described in Section 3.6. During that measurement, the sample is moved away from the focal plane coinciding with the substrate by z-scanning with 10 µm steps, while the intensity of transmitted light is measured. That way, the intensity profile behind the metalens can be visualized and the focusing capability of the metalens can be verified in a direct way. When processing the intensity data, the final intensity profile is calculated as "final data" = "intensity behind the metalens"−"intensity at the substrate".

The intensity profile behind the 5-level HfO_2 metalens, whose nanopillars are all ca. 20 nm shifted in diameter from the ideal size, can be seen in Figure 4.1. The shifted size of the nanostructures should not present a problem since

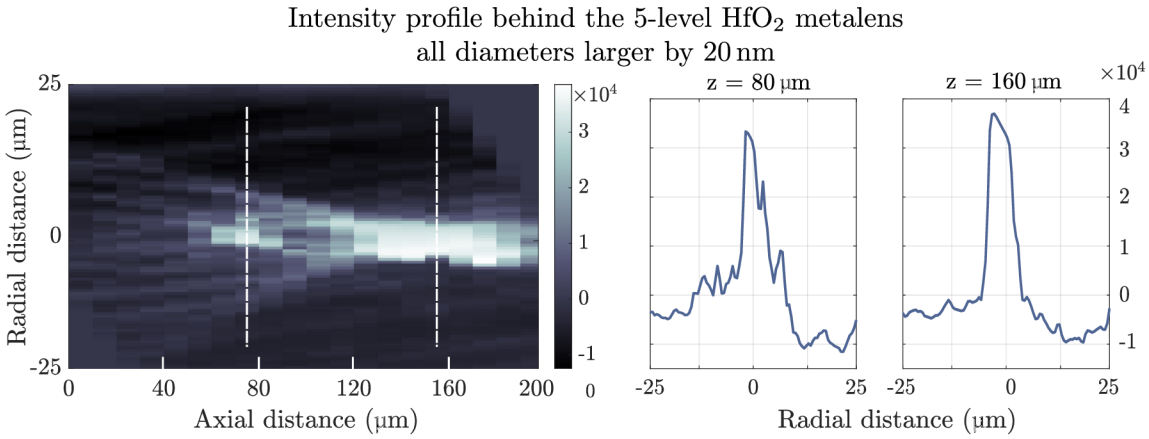

Fig. 4.1: Intensity profile behind the 5-level HfO_2 metalens formed by nanostructures with all diameters larger by 20 nm with respect to the designed sizes. On the left, the z-scan intensity profile is presented. The white dashed lines correspond to two focal spots — minor one at 80 µm and the main one at 160 µm. Lateral intensity profiles at the focal planes can be seen on the right.

the relative phase induced by the nanostructures is kept constant and therefore the phase profile of the lens is sustained. As can be seen in Figure 4.1, the focal point is shifted by 10 µm to 160 µm. Another minor focal spot was observed at 80 µm with slightly lower intensity. This focal point has a sharper spatial profile. In the upper right and the bottom left corner of Figure 4.1, the intensity is uniformly zero due to rotation of the data during processing. The rotation was necessary because the sample was not perfectly parallel during the measurement. The measured intensity profile suggests a significant depth of focus of this metalens, which can be better visualized by the axial intensity profile shown in Figure 4.2.

To demonstrate the robustness of the metalens design, the intensity of imperfect metalenses with fallen-down nanostructures as well as with those hollow cylindrical nanostructures are presented in Figure 4.3. The falling of the nanostructures of the two smallest diameters in 5-level metalens was due to the insufficiently high dose, as was discussed in Section 3.5. Despite the imperfect metalens structure, the focusing capability observed in the intensity profile is still present in the measured data, albeit with the focal point position shifted to 180 µm. The intensity profile of the 5-level metalens formed by hollow nanostructures can be seen in Figure 4.3 on the right: The hollow nanostructures had a significant distorting effect on the intensity profile of the 5-level metalens. This kind of imperfection, compared to the fallen-down nanostructures, prevents an assessment of the focal point presence and hence its position.

As was discussed, the results obtained so far suggest a shift of the main focal point as well as the occurrence of the minor focal point. For proper interpretation of the measured data, a script allowing for theoretical calculation of a beam profile with its phase modulated by a metalens was kindly provided by Ing. Ondřej Červinka (for the script code and further details

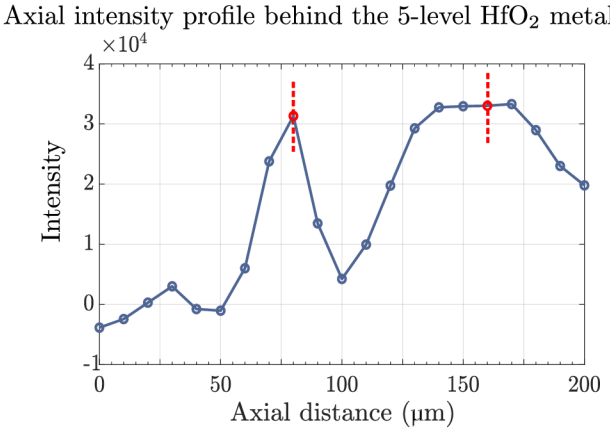

Fig. 4.2: Axial intensity profile of the 5-level metalens, demonstrating the depth of focus. The red dashed lines present the minor and major focal spots of the metalens.

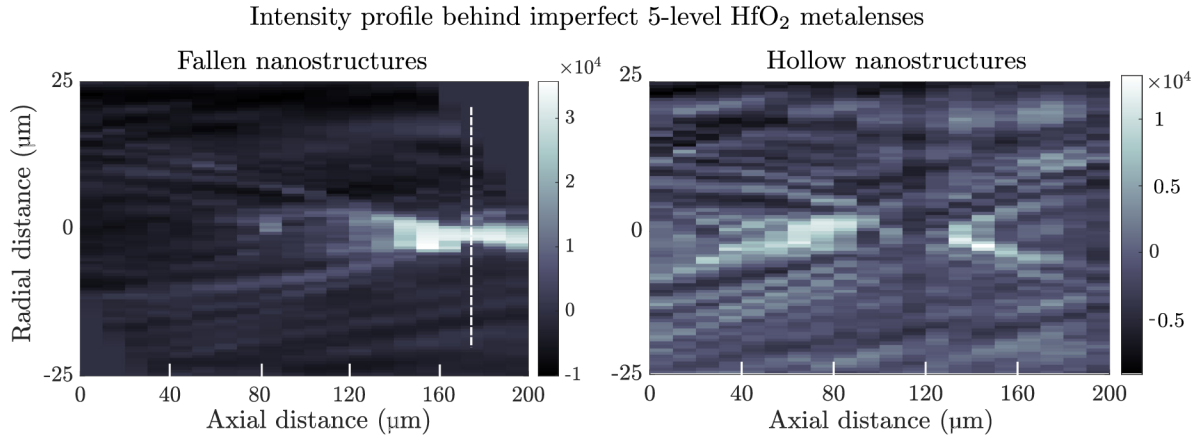

Fig. 4.3: Intensity profiles of imperfect HfO_2 metalenses with fallen-down nanostructures (diameters 80 nm and 104 nm) on the left and hollow nanostructures on the right. The intensity profile o the 5-level metalens with fallen nanostructures shows only a shift in the focal point position. However, for hollow nanostructures, the intensity profile is distorted completely and the focal point can not be assessed.

see Appendix C). As can be seen in Figure 4.4, the ideal smooth lens profile without discretization leads to only one major focal spot, however, for the lens with five discrete levels, the intensity profile is already slightly distorted with the main differences marked by the white rectangle. The intensity profile of a 5-level metalens can be further distorted by multiplying it by a constant. Such a distortion corresponds to fabrication imperfections, where the nanostructures are taller (or shorter) than anticipated, causing steeper (or milder) phase accumulation within each metalens level. As was mentioned in Section 3.5, nanostructures forming the final metalens are ca. (500 ± 10) nm, therefore, the error caused by the imperfect nanopillar height is probable. Distortions of intensity profiles of 5-level metalenses caused by multiplying the phase profile of the 5-level metalens can be seen in Figure 4.5. The results obtained

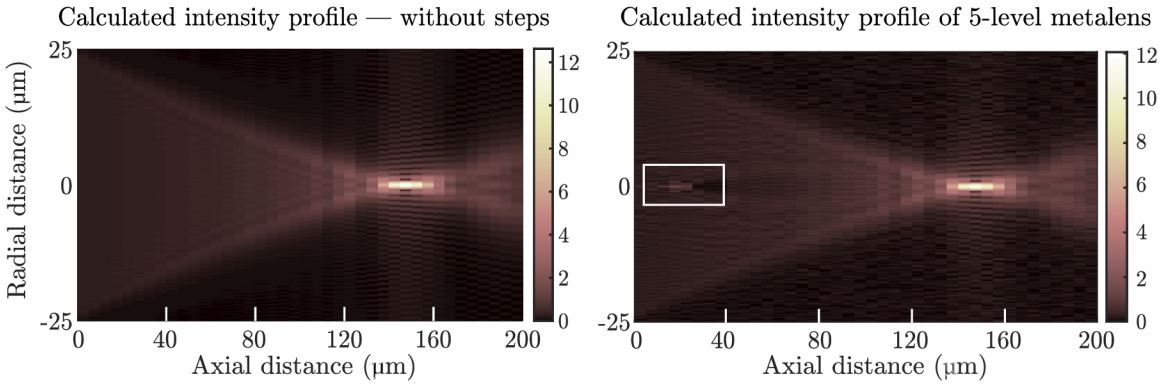

Fig. 4.4: Comparison of calculated intensity profile without steps in phase profile with levelled phase profile for 5-level metalenses. White rectangle marks the distorted area of the intensity profile.

by multiplication error greater than one suggest the existence of the second focal point and are in good agreement with experimentally measured intensity profiles. The occurrence of the minor focal spot of comparable intensity as the main focal spot was present only for the multiplying factors greater than one, which suggests that the nanostructures composing the metalens are taller than 500 nm for which the metalens was designed. To visualize how both of the focal points change with the multiplication error, axial intensity profiles for various multiplication factors are extracted in Figure 4.6. For multiplication errors smaller than one, the intensity of the main focal spot decreases as the multiplication error gets smaller. Interestingly, an almost ideal intensity

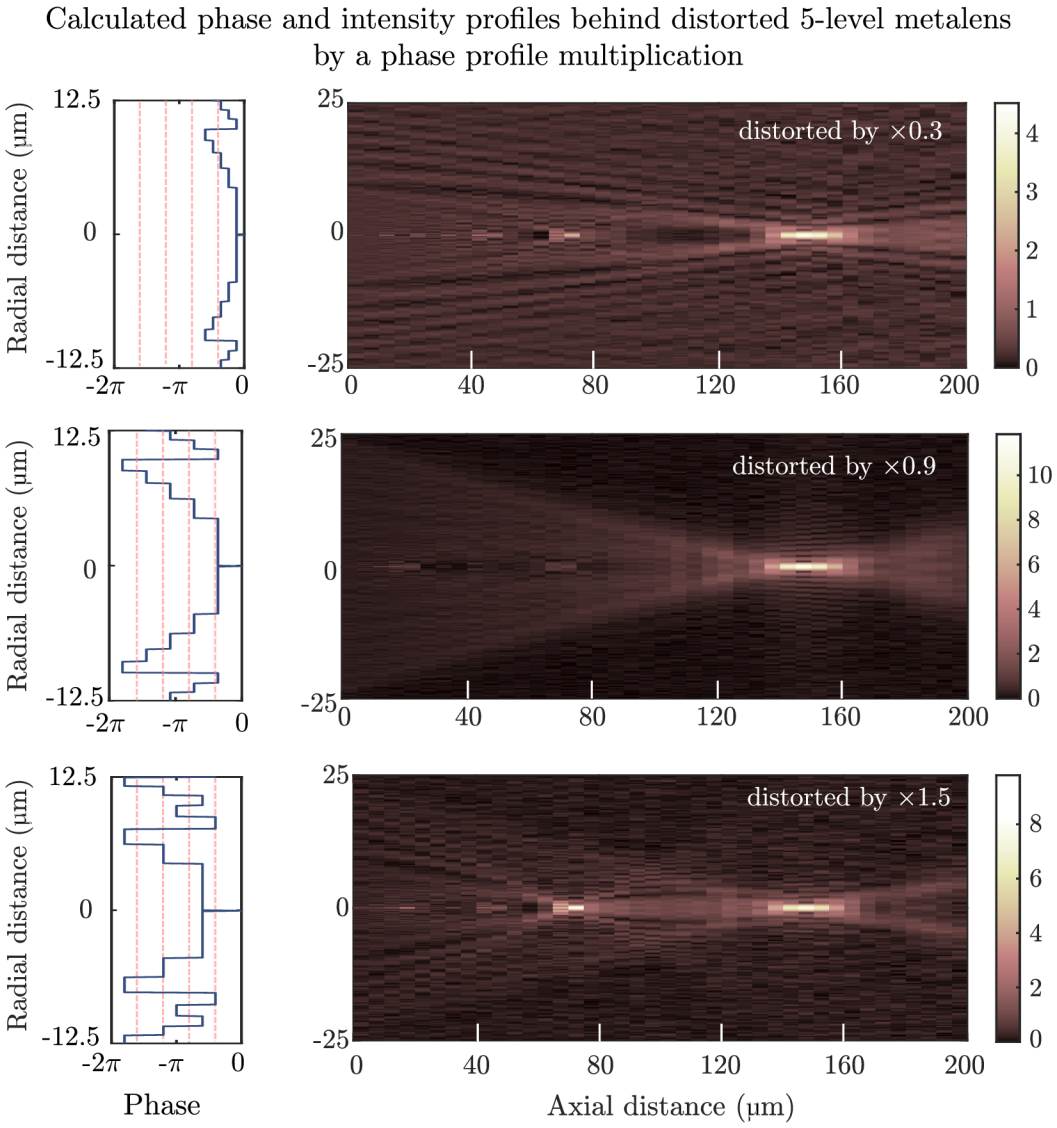

Fig. 4.5: Calculated phase and intensity profiles of 5-level metalenses based on the distorted phase profile by various multiplication errors greater than one. The red dashed line in phase profiles on the left-hand side depicts the ideal phase profile of a 5-level metalens. These calculations verify the occurrence of the minor focal spot, however, the shift of the main focal point was not confirmed.

profile with a minor focal point of low intensity is observed for a multiplication error of 0.9. For multiplication errors greater than one, the intensity between the two focal spots is transferred from the main one to the minor one as the multiplication error gets greater, which can be seen in Figure 4.6 on the right. The multiplication error 1.5 suggest presence of two focal points with a comparable intensity which is in good agreement with the measured 5-level metalens in Figure 4.2. Phase and intensity profiles for all of the distortions in Figure 4.6 are presented in Appendix C. Another way how the unwanted distortion can happen is through the non-ideal phase difference between the levels in the metalens. This error locally disrupts the intensity profile behind the metalens in an area of the intensity profile similar to the one marked by the white rectangle in Figure 4.4. Since the formation of the minor focal spot is not related to this type of distortion, it is thoroughly described in Appendix C. Both of these distorted models show interesting results related mostly to the formation of minor focal spots or local disruption of the intensity profile, however, none of these calculations suggest a shift of the main focal point caused by variation of the nanostructure parameters in terms of their height or diameter. The observed shift in the measured data is most likely caused by the improper calibration of the focus during the z-scanning. Besides the so far discussed 5-level metalens, a 4-level metalens was fabricated and measured as well and the results with thorough description can be found in Appendix B. The main conclusion drawn from these measurements is that the 4-level metalens is more robust towards the imperfections (such as fallen or hollow

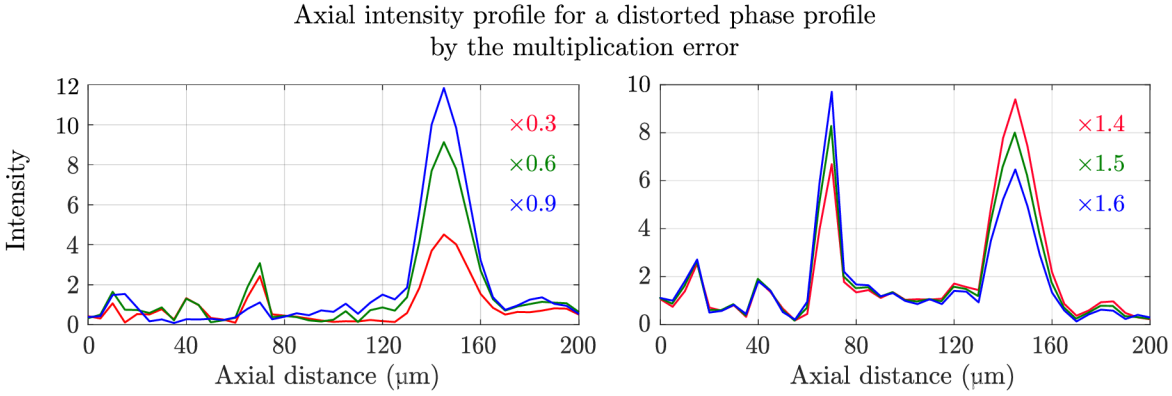

Fig. 4.6: Calculated axial intensity profiles of 5-level metalenses based on the distorted phase profile by various multiplication errors. For multiplication errors smaller than one, the minor spot at 75 µm is of negligible intensity for the ×0.9 multiplication error with only the main focal point at 150 µm whose intensity gets smaller as the multiplication error gets smaller. For multiplication errors greater than one, these calculations show how the intensity is transferred from the main focal spot at 150 µm to the minor focal spot at 75 µm as the multiplication error gets greater. For calculated phase and intensity profiles behind such distorted metalenses see Appendix C.

nanostructures) compared to the 5-level metalens, however, its depth of focus is shallower.

To conclude this chapter, the characterization of 5-level metalens with focal length $f = 150\,\mu m$ was done by mapping of the intensity profile behind the final metalens. The diameters of the meta-atoms were all larger by ca. 20 nm which should not present a problem since the relative phase profile is sustained. For such a lens, the intensity profile with two focal spots was observed — a main one at 160 µm axial distance and a minor one at 80 µm axial distance. Measurements of the imperfect metalenses with fallen-down or hollow nanostructures were shown as well. Based on these measurements it can be concluded that the fallen-down nanostructures did not affect the intensity profile significantly (only the focal point was shifted to 180 µm), however, the hollow nanostructures significantly distorted the intensity profile and the focal point could not be assessed. These results were supported by theoretical calculations in which two different distortions were tested: The first one is by multiplication of the final metalens phase profile which would correspond to utilization of taller/shorter nanostructures in the fabricated metalens. The second one is by adding a difference into a phase levels, which could be intertwined with the proximity effect during the fabrication by EBL. Neither of these calculations estimates the shift of the focal point, however, it was possible to verify the occurrence of the minor focal point most likely due to the employment of taller nanostructures in the fabricated metalens.

Conclusion

UV light plays a crucial role in many applications such as surface sterilization [35], water disinfection [36], medical treatment [37], communication [38], imaging [39], high-resolution photolithography [40] and many more. The conventional optical elements used for the manipulation of UV light so far encounter significant absorption losses, strict limits related to manufacturing precision as well as the overall bulkiness of the optical systems. Following the trend of miniaturization, this work took a closer look at metasurfaces operating at UV wavelengths, presenting metasurface-based counterparts to conventional optical elements such as lenses and holograms. The achievements regarding these elements reported in the literature were compared and discussed based on their efficiency, as well as the material used for their fabrication. Especially in the metaholograms section, the amount of results based on simulations with no experimental verification greatly outweighed the number of works providing fully functional samples. The literature review part was concluded by presenting metasurfaces generating vortex beams as well as metasurfaces made from unconventionally used materials such as diamond or TiO_2 which is usually the material of choice for visible wavelengths. In the literature review, mostly materials from the oxide group (HfO_2, Nb_2O_5, Ta_2O_5) presented functional samples, while materials from the nitride group (AlN, Si_3N_4) remained as simulations only. The need for well-optimized fabrication processes, which is necessary for future implementation of the materials presented only in simulations so far, was stressed throughout the whole literature review.

The practical part of this thesis was dedicated to the fabrication of HfO_2 and AlN metasurfaces. Before the fabrication itself, simulations of the optical response of individual nanopillars used as the meta-atoms were presented. The most important parameter for mimicking the phase profile of the conventional optical counterparts is the phase induced by the nanopillars to the incident light. The simulations were done for both materials, HfO_2 and AlN, for two different wavelengths, 266 nm and 325 nm. With the AlN nanopillars, it was possible to cover the whole phase range with shorter nanostructures (ca. 280 nm) compared to the HfO_2 ones (ca. 450 nm) at both wavelengths. Each material requires a different fabrication approach. The HfO_2 metalens is prepared via ALD into a resist mask previously prepared by EBL into a positive resist. This approach allows for well-controlled nanostructures regarding their height but also the precision of their lateral dimensions. In order to take advantage of the full potential this approach offers, its careful optimization was crucial. The fabrication process for HfO_2 was optimized for nanopillars with circular cross-sections with the smallest diameter being 80 nm and height 500 nm. As a functional sample, the HfO_2 metalens was then successfully fabri-

cated. The other investigated material, AlN, requires etching through a mask during the fabrication process, which is thoroughly described in Appendix A. During the optimization, approaches involving Cr hard mask fabricated through EBL and lift-off as well as a negative resist were tested. Unfortunately, due to a very low directionality of the tested etching recipes in chlorine RIE, a functional sample based on the AlN material platform was not demonstrated. As a functional sample metalens formed by HfO_2 nanostructures was chosen. Designing of the metalens was demonstrated on 4- and 5-level metalenses with focal distance $f = 150\,\mu m$ and numerical aperture NA = 0.3, employing the previously simulated HfO_2 nanostructures.

The final chapter of this work presented the characterization of 5-level HfO_2 metalenses in a custom-made optical setup which allows for mapping the intensity profiles behind the metalenses. The results obtained by these measurements suggest presence of two various focal points of the 5-level metalens. The main focal point was shifted to 160 µm (from the designed 150 µm), while the minor one appeared at 80 µm. The experimentally obtained data were compared to theoretically calculated intensity profiles which were distorted either by adding or subtracting errors of phase steps or by multiplication of the final phase profile by an error factor. The calculated intensity profiles obtained by the multiplication error greater than one, which show a second focal point with comparable intensity as the main one, were in good agreement with the measured data — this suggested that the fabricated nanostructures are in fact taller than those required by the design. To demonstrate the robustness of the metasurface approach, intensity profiles of metalenses with fallen-down and hollow nanostructures were also measured. For the 5-level metalens with fallen-down nanostructures, the intensity profile was sustained with a shift of the focal point to 180 µm. However, for the metalens with hollow nanostructures the intensity profile was highly distorted, disabling the assessment of the position of the focal point. Measurements done on 4-level metalenses are summarized in Appendix B and their main advantage over 5-level metalenses turned out to be greater robustness towards imperfections. This was concluded from the fact that for both metalenses with fallen-down and hollow nanostructures, the assessment of the position of the focal point was possible, contrary to the 5-level metalens.

Results presented in this work were not the first results based on the HfO_2 material platform used for metalens fabrication. However, insights obtained from the thorough optimization of the fabrication process as well as the theoretical calculations of the metalens profiles present a reliable base for the design and fabrication of metasurfaces suitable for UV.

A AlN fabrication

In this text, the steps taken towards the fabrication optimization of AlN nanostructures will be described. For the fabrication of AlN metasurface, two different approaches schematically depicted in Figure A.1 were tested. Both of these approaches start with the deposition of AlN onto a fused silica substrate in the first step. The first approach, described in the upper branch of Figure A.1, employs EBL into a positive resist, forming holes of the desired design which are consequently filled with a future hard-mask material — here, with chromium (Cr). The Cr nanostructures on the AlN surface then serve as the hard mask over which the etching is done. The etching can be purely physical, employing argon ion beam etching, or also chemical, employing RIE. In order to get the final metasurface, Cr capping must be removed in the last step. The second approach, described in the bottom branch of Figure A.1, employs EBL into a negative resist, which then forms the etching mask by itself after the development. After that, the AlN is etched again by one of the previously mentioned etching techniques. In the final step, the negative resist capping must be removed to obtain the final metasurface.

The deposition of the AlN was done by Dr. Imrich Gablech, who previously published an article on such deposition [97]. The thickness of the AlN film was measured to be 290 nm via profilometer by Dr. Imrich Gablech as well. This thickness is sufficient for the fabrication of nanostructures, which allow for complete freedom in the manipulation of the incident light of 266 nm

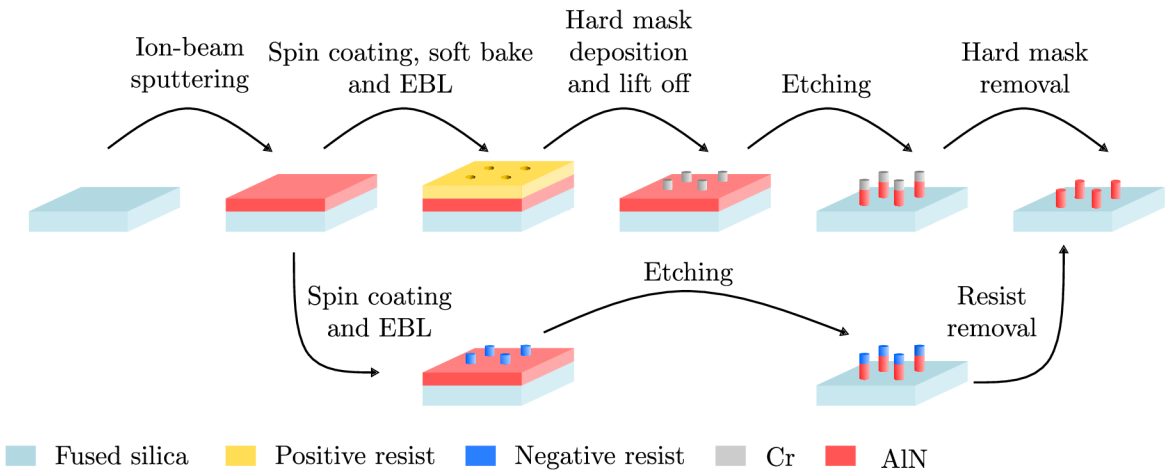

Fig. A.1: Scheme of the fabrication process of AlN nanostructures both of which start with the AlN deposition as the first step. The upper branch presents the approach, which uses Cr hard mask fabricated via lift-off. The Cr mask is then used as an etching mask and the final AlN metasurface is obtained after the Cr capping removal by wet etching of Cr. The bottom branch uses negative resist as an etching mask, where the final metasurface is as well obtained after the etching and resist removal.

wavelength for nanostructures with constant spacing $P = 150\,\text{nm}$, as is shown by the simulations done by Ing. Peter Kepič in Figure A.2

In the hard mask approach, the most important factor of the fabrication is the etching through the hard mask. The hard mask is formed in the first step by EBL into a positive resist, using adhesion promoter (AR 300-80 [88]), positive resist (6200.09 [89]) and polymerous conductive layer (5090.02 [91]), see the application parameters summarized in Table A.1. The dose test design for lithography, as can be seen in Figure A.3, was composed of $(20\times20)\,\mu\text{m}^2$ arrays with nanostructure sizes (55, 70, 80, 85, 95, 105, 115 and 130) nm and with constant spacing $P = 150\,\text{nm}$. The doses varied from $100\,\mu\text{C/cm}^2$ to $200\,\mu\text{C/cm}^2$, with steps of $10\,\mu\text{C/cm}^2$. For the patterning, 20 kV acceleration voltage, 15 µm aperture (corresponding to current around 65 pA) and $(40 \times 40)\,\mu\text{m}^2$ write field size were used. After the resist development in AR 600-546 for 60 s and in isopropyl alcohol for 30 s the holes in the resist were filled with Cr to form a hard mask. The Cr deposition is followed by a so-called lift-off during which the sample is soaked in the resist remover (dioxolane), resulting also in the removal of the Cr on top of the resist. The final Cr hard mask served as an etching mask for the subsequent RIE by chlorine gases in Oxford Instruments Plasma Technology PlasmaPro 100. The RIE recipe is composed of two steps: The first one is a breakthrough of the potential oxide layer, which could form on the sample surface, when the surface is exposed to laboratory atmosphere. The second step is the main etching process. The parameters of etching for two different tests, which varied both in thickness of the Cr hard mask and in parameters of the etching process, are shown in Table A.1b,c. The power of the inductively coupled plasma (ICP) source, (ensuring the creation of ions) and the power of the RIE source accelerating the ions towards the sample surface were kept the same for both of the tests, as well as the the pressures during the breakthrough and main etch step. The results based on these etching

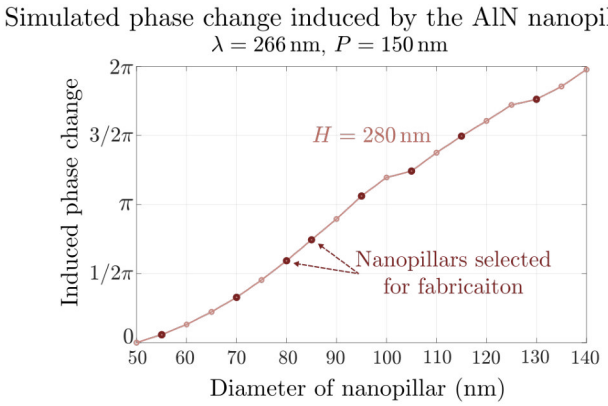

Fig. A.2: The first simulations supporting the fabrication of AlN nanopillars of height 280 nm and with constant spacing 150 nm done by Ing. Peter Kepič. The selected nanopillars of various diameters are marked by full red circles.

parameters with two different mask thicknesses are shown in Figure A.3b: Each column represents Cr hard mask of a certain diameter of either 40 nm or 90 nm thickness from the top view and after etching. As can be seen there, the 40 nm Cr hard mask seems to be insufficient for the etching of the nanostructures which manifested as short and wide nanostructures regardless of Cr hard mask diameter. After increasing Cr thickness to 90 nm and changing the ratio of the gases during the main etching, the resulting nanostructures were a little bit narrower. It also seems that the diameters of the etched nanostructures are all the same regardless of the diameter of the Cr hard mask. From the etching parameters it seems, that with an increase of argon ions, the sidewall profile of the nanostructures was a bit more vertical. However, when solely argon ion etching was tested for a Cr mask of 100 nm thickness, the AlN was etched down completely, most likely because Cr has a higher sputter yield. This problem could be solved by using a different material, such as titanium, for the hard mask, however, the biggest advantage of Cr is that it can be removed after the etching in the Cr wet etchant TechniEtch Cr01 [92] which has a negligible etch rate for AlN and therefore would not greatly affect the nanostructures. Overall, increasing the thickness of the Cr hard mask did not show promising

Tab. A.1: Summary of parameters used during preparation and etching of the AlN metasurfaces

a) Parameters used for the hard mask fabrication

Product	Spin coating and soft bake parameters	Product info
AR 300-80	4000 rpm/ 2000 rpms/ 60 s and 180 °C/ 120 s	[88]
AR-P 6200.09	4000 rpm/ 2000 rpms/ 60 s and 150 °C/ 60 s	[89]
AR-PC 5090.02	2000 rpm/ 500 rpms/ 60 s and 90 °C/ 180 s	[91]

b) Etching parameters of sample with 40 nm Cr hard mask

Step	Gases and flows	Duration	ICP	RIE	Pressure
Breakthrough	BCl_3/ 15 sccm	30 s	200 W	150 W	8 mTorr
Main etch	Cl_2/ 12 sccm and Ar/ 10 sccm	4.5 min	200 W	150 W	12 mTorr

c) Etching parameters of sample with 90 nm Cr hard mask

Step	Gases and flows	Duration	ICP	RIE	Pressure
Breakthrough	BCl_3/ 15 sccm	10 s	200 W	150 W	8 mTorr
Main etch	Cl_2/ 10 sccm and Ar/ 30 sccm	5 min	200 W	150 W	12 mTorr

d) Negative resist spin coating

Product	Spin coating and soft bake parameters	Product info
AR-N 7520.07	4000 rpm/ 2000 rpms/ 60 s and 85 °C/ 60 s	[98]

results based on the nanostructure shapes for both RIE and argon ion etching. Therefore, the second approach where the negative resist is used as the etching mask was tested.

The second approach employed negative resist (AR-N 7520.07 [98]), whose spin coating and soft bake parameters are noted in Table A.1d. The EBL had the same design as the previous one except the doses varied from 30 µC/cm^2 to 180 µC/cm^2. The negative resist was developed by tetramethylammonium hydroxide for 50 s and the development was stopped by 30 s submerge in deionized water. The durability of the resist towards ion etching was improved by the soft bake after the resist development at 85 °C for 60 s, as suggested by the product information [98]. The negative resist after patterning and development can be seen in Figure A.4. The diameter of the smallest nanostructures, which was possible to obtain via patterning the negative resist was ca. 70 nm. Both RIE and argon ion etching were tested, however, the resist mask did not last out and hence there were no nanostructures to be observed afterwards.

Based on the previous unsuccessful results, the final try was given to the combination of both approaches, where a 100 nm thick Cr layer is deposited

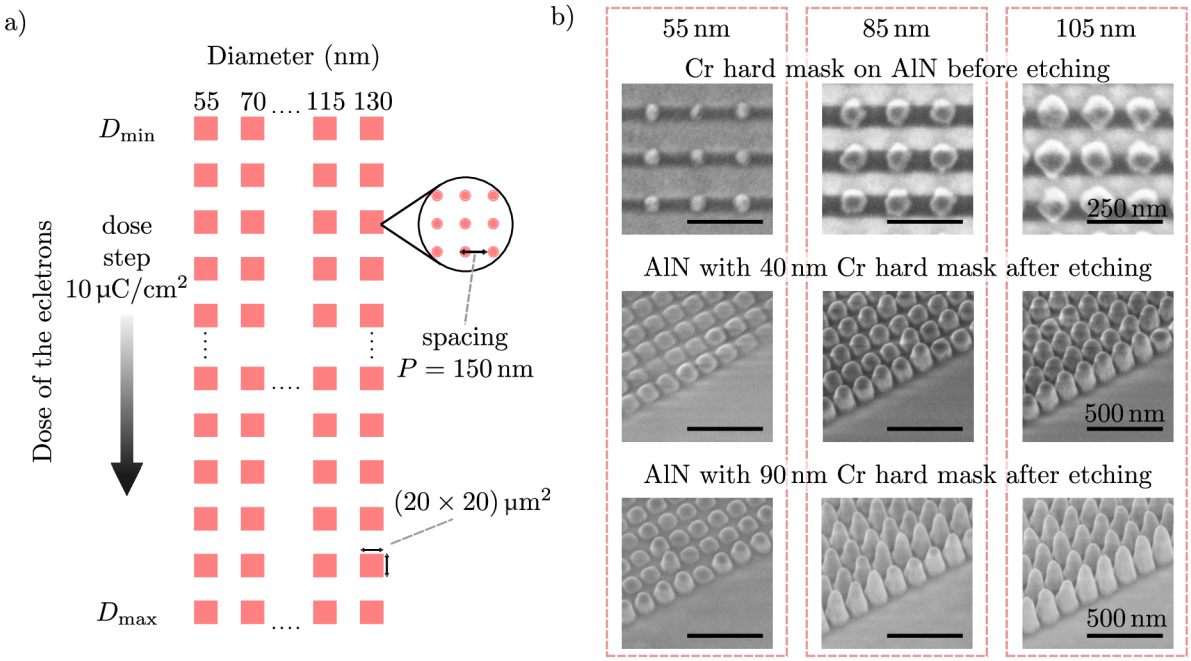

Fig. A.3: a) The layout of the dose test design with varying diameters in each column and dose in each row by step 10 µC/cm^2 used for both fabrication of Cr hard mask as well as for the fabrication of negative resist mask with varying minimum (D_{min}) and maximum (D_{max}) dose. b) SEM images of Cr hard mask of various diameters before etching as well as after two different etching recipes. The second row presents nanostructures after etching over 40 nm Cr hard mask where the main etch consists of Cl_2/ 12 sccm flow and Ar/ 10 sccm flow. The third row presents nanostructures after etching over 90 nm Cr hard mask with the main etching combining Cl_2/ 10 sccm and Ar/ 30 sccm, making the etching rather physical than chemical.

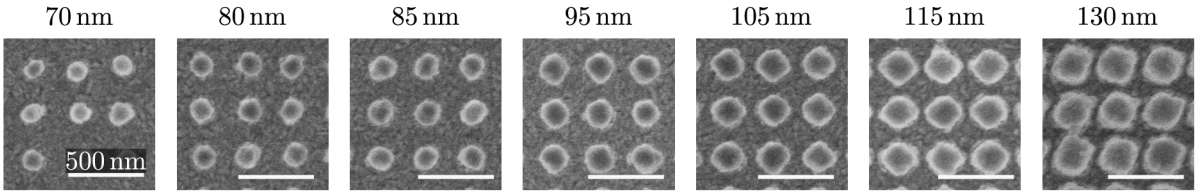

Fig. A.4: SEM images of the negative resist after development, the mask diameters are written above each SEM image. It was possible to obtain resist mask with the smallest diameter 70 nm. The subsequent etching was unsuccessful due to the negative resist did not withstand both the RIE and ion beam etching.

on top of the AlN and then the EBL into the negative resist is carried out. After the resist development, the Cr is etched in RIE by chlorine gases and the final etch over a double mask formed by Cr and the negative resist is done by ion beam etching. Unfortunately, as can be seen in the previous chapter related to methods in Section 3.4, both Cr and resist are etched by oxygen, therefore, during the chromium etching, the resist was removed completely and this approach was not possible to test.

Since the fabrication optimization of AlN nanostructures was unsuccessful, the functional metasurface based on the AlN material platform will not be demonstrated. Mainly due to the time-consuming optimization with a very little yield of presentable results, the fabrication optimization of the AlN nanostructures is left for future study. Based on the results reached so far where the nanostructures are almost of the same diameter regardless of the diameter of the mask, it might be better to employ only a rectangular nanostructure of a certain length and width and achieve freedom in phase manipulation of the incident light via geometric phase. It was shown in the literature that it is possible to grow AlN nanostructures via combination of preferential crystallization with dry etching and metal organic vapour phase epitaxy [99] or AlN nanowires via arc discharge [100]. Other results reported are mostly unorganized nanostructures, such as nanotips and nanorods [101].

B 4-level HfO_2 metalens

The following text describes (in a similar nature as was done for 5-level metalens in Chapter 4) characterization of 4-level HfO_2 metalenses with designed focal length $f = 150\,\mu m$. The intensity profile behind the 4-level metalens can be seen in Figure B.1: Two different focal points are present in this intensity profile — focal points at $100\,\mu m$ (referred to as minor) and at $140\,\mu m$ (referred to as main) of comparable intensities. The main focal point is slightly shifted from the designed position of $150\,\mu m$. The axial intensity profile behind such a metalens can be seen in Figure B.2, where the red dashed lines mark position of the focal points. The depth of focus suggested from the axial profile is lower compared to the 5-level metalens. However, the robustness of the 4-level metalens is much better compared to the 5-level metalens, which can be demonstrated on the intensity profiles shown in Figure B.3. As can be seen there, for both metalenses with fallen and hollow nanostructures, it

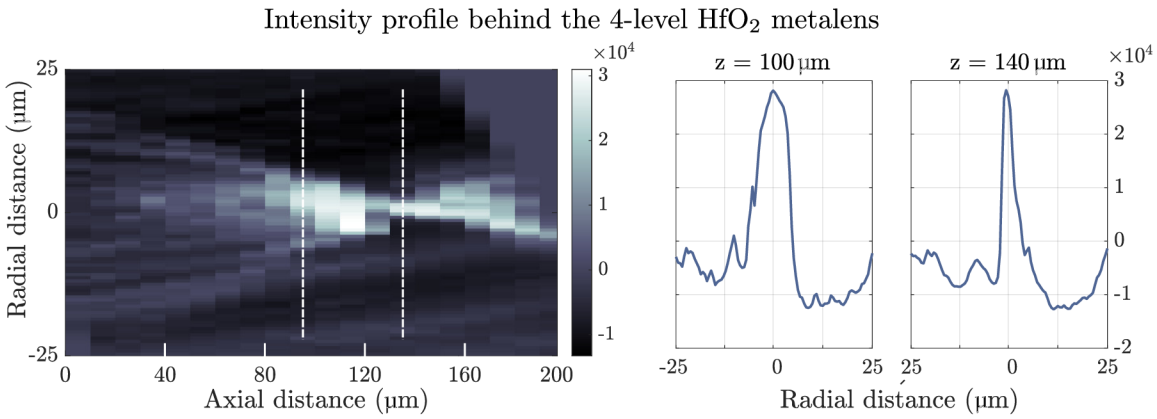

Fig. B.1: Intensity profile of 4-level HfO_2 metalens. On the left-hand side, the z-scan intensity profile is presented. The white dashed corresponds to a focal spots at $100\,\mu m$ and $140\,\mu m$ whose intensity profiles can be seen on the right-hand side.

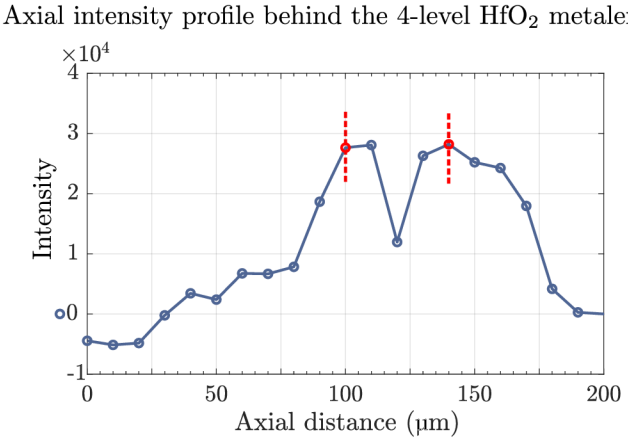

Fig. B.2: Axial intensity profile of the 4-level metalens, demonstrating well the depth of focus. The red dashed lines present the focal spots of the metalens.

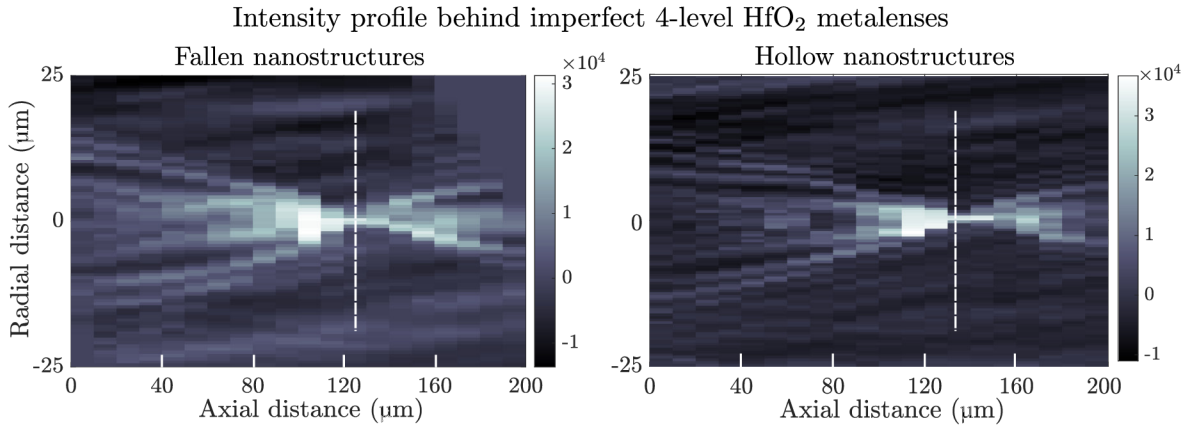

Fig. B.3: Intensity profiles of imperfect HfO_2 metalenses with fallen-down nanostructures (diameters 80 nm and 108 nm) on the left-hand side and hollow nanostructures on the right-hand side. Both of the intensity profiles suggest only shift of the focal point position.

is possible to asses the focal point and its position. The focal point of the metalens with fallen nanostructures is shifted to 120 µm. The focal point of the metalens with hollow nanostructures is still observable (compared to the 5-level metalens for which the focal point was not possible to assess) at 130 µm. So far for all of the intensity profiles, the shift in the focal point compared to the designed position was discussed. However, as was already mentioned in Chapter 4, this behaviour was not confirmed by the theoretical calculations of distorted metalens profiles by either phase multiplication nor phase difference in the levels of the metalens. On the other hand, these calculation verified the occurrence of the second focal point, which is intertwined with the taller fabricated nanostructures compared to those used in the metalens design.

C Theoretical calculations

The following text describes the theoretical calculations of the phase distortion, which were discussed in Chapter 4. The main script of these calculations (the phase profile and its intensity projection done via Fourier transform) was kindly provided by Ing. Ondřej Červinka. The phase profile is calculated as:

```
1 wavelength = 0.325;
2 f = 150;
3 %%calculated area setup for 50x50 um2 field
4 dx=0.05;
5 dy=dx;
6 [x,y] = meshgrid([-25:dx:25],[-25:dx:25]);
7 %%two different ways of phase profile distortion
8 step_difference = 0
9 multiplication_error=1
10 %%calculation of phase profile without steps
11 phase_profile = -(2*pi*(sqrt(x.^2+y.^2+f.^2)-f))/wavelength;
12 %%obtaining phase only from 0 to 2pi - returns the remainder
       after 2pi division
13 phase_profile = rem(phase_profile,2*pi);
14 %%size of a phase step in each lens level
15 phase_step = 2*pi/5+step_difference;
16 %%calculation of final phase profile of the levelled metalens
17 phase_profile = rem(phase_step*floor(phase_profile/phase_step)*
       multiplication_error,2*pi);
```

The first distortion was done via multiplication of the final metalens phase profile by multiplication error defined on line 9 and applied on the final phase profile on line 17. The second distortion was done via alteration of the difference in steps is done via adding or subtracting the step difference defined on line 8 and applied on line 15. In the above-mentioned script, the distortion caused by a step difference is set to zero and the multiplication is set to one, which corresponds to the ideal 5-level metalens profile.

In Chapter 4 multiplication of the final phase profile for various multiplication errors was shown in the form of the axial intensity profiles. Here, phase profiles as well as intensity profiles behind such distorted metalenses for multiplying errors both smaller and greater than one are shown in Figures C.1 and C.2. For the multiplication error smaller than one, the inability of covering the whole range from 0 to 2π is visible in the phase profile graphs on the left-hand side of Figure C.1. This has a direct impact on the focusing efficiency, manifesting as higher intensity levels around the focal point region. For multiplication errors greater than one, the intensity and phase profiles are depicted in Figure C.2. To compare both of the cases, it is advantageous to

take a closer look at the minor focal point which occurs at around 75 µm axial distance. Its intensity is lower for distortion by multiplication error smaller than one compared to the case, where the intensity profile was distorted by multiplication errors greater than one. By comparison of the experimentally measured data with the intensity profile calculations, a better agreement was found for multiplication errors greater than one, suggesting that the fabricated nanostructures are taller than the ones in the 5-level metalens design.

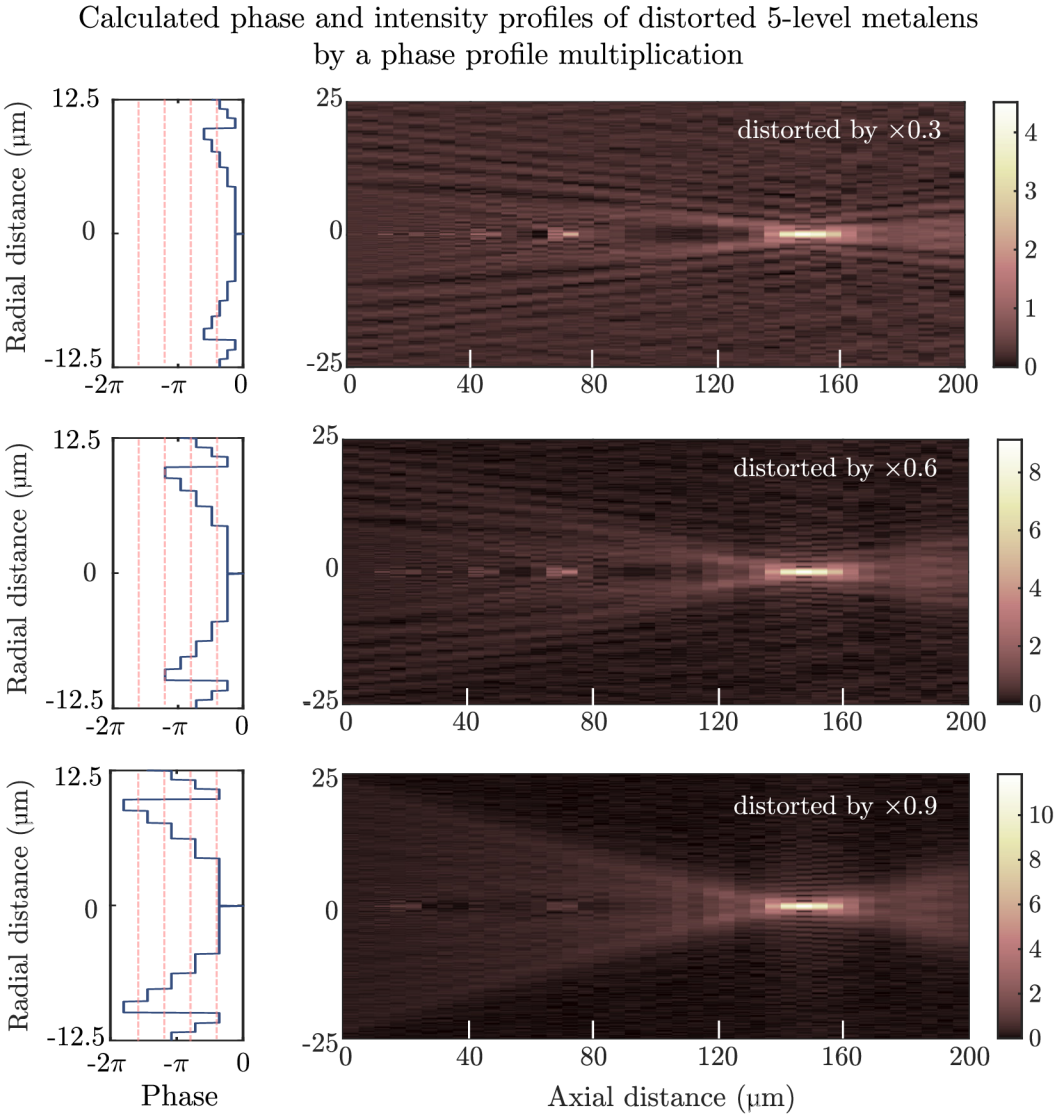

Fig. C.1: Calculated phase and intensity profiles of 5-level metalenses based on the distorted phase profile by various multiplication errors smaller than one. The red dashed line in phase profiles on the left-hand side depicts the ideal phase profile of a 5-level metalens. The observed minor focal spot at 75 µm is of smaller intensity compared to the case where the multiplication error was greater than one. These results are not in good agreement with the experimentally measured data, regarding the focusing efficiency and intensity of the minor focal point

The distortion caused by the step difference can be seen in Figure C.3 for three different factors. This can be manifested in fabrication as a change of the diameters of given nanostructures, which may be caused by the proximity effect during EBL (see Section 3.2). Based on the calculations of the phase and intensity profile of 5-level metalens in Figure C.3, which are distorted by various differences in levels, we can see that this mainly affects the number of steps in the phase profile behind the final metalens. This affects the local disruption of the intensity profile — the finer the profile's steps, the smaller the

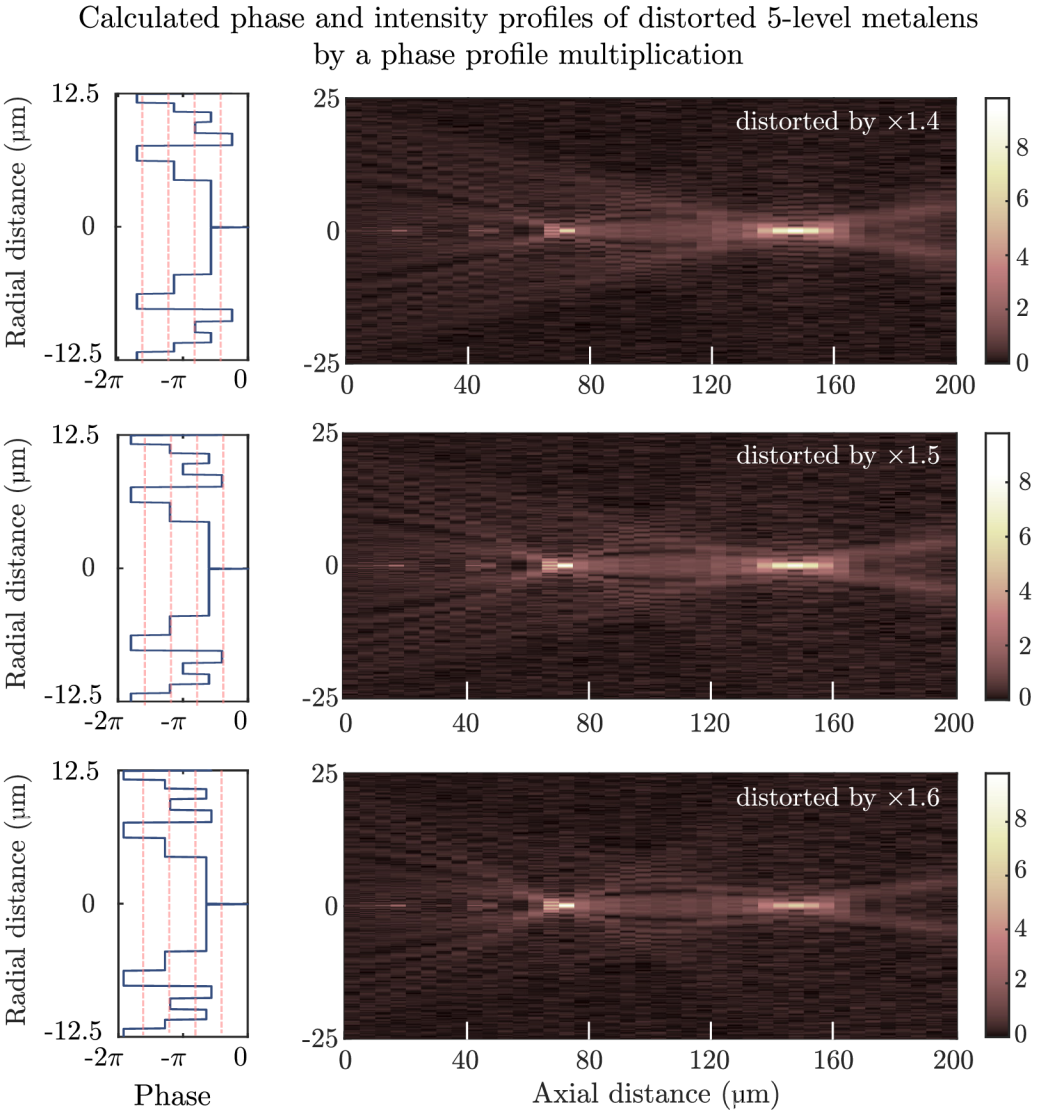

Fig. C.2: Calculated phase and intensity profiles of 5-level metalenses based on the distorted phase profile by various multiplication errors greater than one. The red dashed line in phase profiles on the left-hand side depicts the ideal phase profile of a 5-level metalens. The observed minor focal spot at 75 µm is of greater intensity compared to the case where the multiplication error was smaller than one. These results are in good agreement with the experimentally measured data, regarding the intensity of the minor focal point

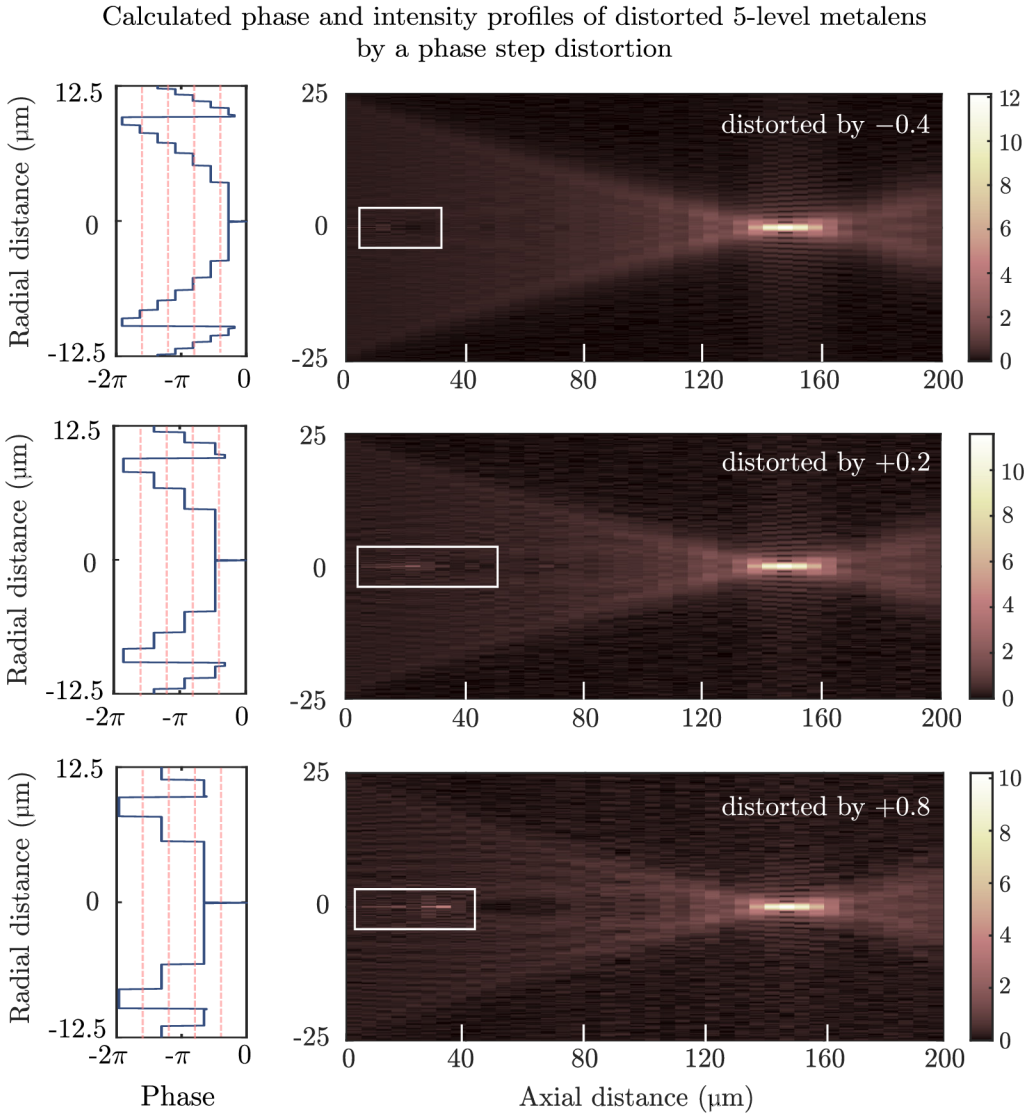

Fig. C.3: Calculated phase and intensity profiles of 5-level metalenses based on the distorted phase profile by variation of the difference in the levels. The red dashed line in phase profiles on the left-hand side depicts the ideal phase profile of a 5-level metalens. These calculations suggest that the slight local disruption of intensity profile (inherent to the 5-level metalens) worsens, as the number of levels decreases.

intensity profile's disruption (marked by white rectangles). It is important to note, that the region of the intensity disruption caused by the levels differences is around the same position as observed inherently in the ideal 5-level metalens intensity profile (see Chapter 4, Figure 4.4).

Bibliography

[1] K. Miyamoto. "The Phase Fresnel Lens". *Journal of the Optical Society of America*. vol. 51. no. 1, p. 17. Jan. 1961. DOI: 10.1364/JOSA.51.000017.

[2] P. Genevet et al. "Recent advances in planar optics: From plasmonic to dielectric metasurfaces". *Optica*. vol. 4, p. 139. 1 Jan. 2017. DOI: 10.1364/OPTICA.4.000139.

[3] J. Engelberg et al. "The advantages of metalenses over diffractive lenses". *Nature Communications*. vol. 11, p. 1991. 1 Apr. 2020. DOI: 10.1038/s41467-020-15972-9.

[4] J. Wang et al. "Plasmonic and dielectric metasurfaces: Design, fabrication and applications". *Applied Sciences*. vol. 6, p. 239. 9 Sep. 2016. DOI: 10.3390/app6090239.

[5] S. A. Maier. *Surface Plasmon Polaritons at Metal / Insulator Interfaces*. Springer US, 2007, pp. 21–37. DOI: 10.1007/0-387-37825-1_2.

[6] M. A. Kats et al. "Effect of radiation damping on the spectral response of plasmonic components". *Optics Express*. vol. 19, p. 21 748. 22 Oct. 2011. DOI: 10.1364/OE.19.021748.

[7] N. Yu et al. "Light propagation with phase discontinuities: Generalized laws of reflection and refraction". *Science*. vol. 334, pp. 333–337. 6054 Oct. 2011. DOI: 10.1126/science.1210713.

[8] S. Jahani et al. "All-dielectric metamaterials". *Nature Nanotechnology*. vol. 11, pp. 23–36. 1 Jan. 2016. DOI: 10.1038/nnano.2015.304.

[9] A. I. Kuznetsov et al. "Optically resonant dielectric nanostructures". *Science*. vol. 354. 6314 Nov. 2016. DOI: 10.1126/science.aag2472.

[10] J. Li et al. "Mechanisms of 2π phase control in dielectric metasurface and transmission enhancement effect". *Optics Express*. vol. 27, p. 23 186. 16 Aug. 2019. DOI: 10.1364/OE.27.023186.

[11] A. Niv et al. "Manipulation of the pancharatnam phase in vectorial vortices". *Optics Express*. vol. 14, p. 4208. 10 2006. DOI: 10.1364/OE.14.004208.

[12] M. Kerker et al. "Electromagnetic scattering by magnetic spheres". *Journal of the Optical Society of America*. vol. 73, p. 765. 6 Jun. 1983. DOI: 10.1364/JOSA.73.000765.

[13] M. Khorasaninejad et al. "Metalenses at visible wavelengths: Diffraction-limited focusing and subwavelength resolution imaging". *Science*. vol. 352, pp. 1190–1194. 6290 Jun. 2016. DOI: 10.1126/science.aaf6644.

[14] Y. F. Yu et al. "High-transmission dielectric metasurface with 2 phase control at visible wavelengths". *Laser & Photonics Reviews*. vol. 9, pp. 412–418. 4 Jul. 2015. DOI: 10.1002/lpor.201500041.

[15] M. Khorasaninejad et al. "Silicon nanofin grating as a miniature chirality-distinguishing beam-splitter". *Nature Communications*. vol. 5, p. 5386. 1 Nov. 2014. DOI: 10.1038/ncomms6386.

[16] S. Sun et al. "All-dielectric full-color printing with tio ₂ metasurfaces". *ACS Nano*. vol. 11, pp. 4445–4452. 5 May 2017. DOI: 10.1021/acsnano.7b00415.

[17] Y. Hu et al. "All-dielectric metasurfaces for polarization manipulation: Principles and emerging applications". *Nanophotonics*. vol. 9, pp. 3755–3780. 12 Sep. 2020. DOI: 10.1515/nanoph-2020-0220.

[18] M. I. Shalaev et al. “High-efficiency all-dielectric metasurfaces for ultracompact beam manipulation in transmission mode”. *Nano Letters*. vol. 15, pp. 6261–6266. 9 Sep. 2015. DOI: 10.1021/acs.nanolett.5b02926.

[19] “Microscopy by reconstructed wave-fronts”. *Proceedings of the Royal Society of London. Series A. Mathematical and Physical Sciences*. vol. 197. no. 1051, pp. 454–487. Jul. 1949. DOI: 10.1098/rspa.1949.0075.

[20] G. Tricoles. “Computer generated holograms: An historical review”. *Applied Optics*. vol. 26, p. 4351. 20 Oct. 1987. DOI: 10.1364/AO.26.004351.

[21] L. Huang et al. “Metasurface holography: From fundamentals to applications”. *Nanophotonics*. vol. 7, pp. 1169–1190. 6 Jun. 2018. DOI: 10.1515/nanoph-2017-0118.

[22] J. P. B. Mueller et al. “Metasurface polarization optics: Independent phase control of arbitrary orthogonal states of polarization”. *Physical Review Letters*. vol. 118, p. 113 901. 11 Mar. 2017. DOI: 10.1103/PhysRevLett.118.113901.

[23] M. A. Ansari et al. “Engineering spin and antiferromagnetic resonances to realize an efficient direction-multiplexed visible meta-hologram”. *Nanoscale Horizons*. vol. 5, pp. 57–64. 1 2020. DOI: 10.1039/C9NH00460B.

[24] M. L. Tseng et al. “Metalenses: Advances and applications”. *Advanced Optical Materials*. vol. 6, p. 1 800 554. 18 Sep. 2018. DOI: 10.1002/adom.201800554.

[25] M. Pan et al. “Dielectric metalens for miniaturized imaging systems: Progress and challenges”. *Light: Science & Applications*. vol. 11, p. 195. 1 Jun. 2022. DOI: 10.1038/s41377-022-00885-7.

[26] R. C. Devlin et al. “Broadband high-efficiency dielectric metasurfaces for the visible spectrum”. *Proceedings of the National Academy of Sciences*. vol. 113, pp. 10 473–10 478. 38 Sep. 2016. DOI: 10.1073/pnas.1611740113.

[27] Z. Wang et al. “A high numerical aperture terahertz all-silicon metalens with sub-diffraction focus and long depth of focus”. *Journal of Physics D: Applied Physics*. vol. 54, p. 085 103. 8 Feb. 2021. DOI: 10.1088/1361-6463/abc3ee.

[28] M. Melli et al. “Gallium phosphide optical metasurfaces for visible light applications”. *Scientific Reports*. vol. 10, p. 20 694. 1 Nov. 2020. DOI: 10.1038/s41598-020-77753-0.

[29] M. Khorasaninejad et al. “Metalenses at visible wavelengths: Diffraction-limited focusing and subwavelength resolution imaging”. *Science*. vol. 352, pp. 1190–1194. 6290 Jun. 2016. DOI: 10.1126/science.aaf6644.

[30] J. Y. Lee et al. “All dielectric metasurface nano-fabrication based on tio2 phase shifters”. E. M. Campo et al., Eds. SPIE, Aug. 2017, p. 17. DOI: 10.1117/12.2272148.

[31] T. Hu et al. “Cmos-compatible a-si metalenses on a 12-inch glass wafer for fingerprint imaging”. *Nanophotonics*. vol. 9, pp. 823–830. 4 Apr. 2020. DOI: 10.1515/nanoph-2019-0470.

[32] “Johann wilhelm ritter”. (2023). [Online]. Available: https://www.britannica.com/biography/Johann-Wilhelm-Ritter.

[33] P. E. Hockberger. “A History of Ultraviolet Photobiology for Humans, Animals and Microorganisms”. *Photochemistry and Photobiology*. vol. 76. no. 6, pp. 561–579. May 2007. DOI: 10.1562/0031-8655(2002)0760561AHOUPF2.0.CO2.

[34] D. Zhao et al. “Recent advances in ultraviolet nanophotonics: From plasmonics and metamaterials to metasurfaces”. *Nanophotonics*. vol. 10, pp. 2283–2308. 9 Jul. 2021. DOI: 10.1515/nanoph-2021-0083.

[35] C. C. R. Ramos et al. “Use of ultraviolet-C in environmental sterilization in hospitals: A systematic review on efficacy and safety”. *International Journal of Health Sciences*. vol. 14. no. 6, pp. 52–65. 2020.

[36] K. Song et al. “Application of ultraviolet light-emitting diodes (UV-LEDs) for water disinfection: A review”. *Water Research*. vol. 94, pp. 341–349. May 2016. DOI: 10.1016/j.watres.2016.03.003.

[37] V. Kozobolis et al. “UV-A Collagen Cross-Linking Treatment of Bullous Keratopathy Combined With Corneal Ulcer”. *Cornea*. vol. 29. no. 2, pp. 235–238. Feb. 2010. DOI: 10.1097/ICO.0b013e3181a81802.

[38] L. Guo et al. “Ultraviolet communication technique and its application”. *Journal of Semiconductors*. vol. 42. no. 8, p. 081 801. Aug. 2021. DOI: 10.1088/1674-4926/42/8/081801.

[39] J. Østergaard. “UV imaging in pharmaceutical analysis”. *Journal of Pharmaceutical and Biomedical Analysis*. vol. 147, pp. 140–148. Jan. 2018. DOI: 10.1016/j.jpba.2017.07.055.

[40] “Extreme uv photolithography”. (2023). [Online]. Available: https://www.newport.com/n/extreme-uv-photolithography.

[41] “Uv optics: Tighter tolerances and different materials”. (2022). [Online]. Available: https://www.edmundoptics.eu/knowledge-center/application-notes/lasers/uv-optics-tighter-tolerances-and-different-materials/..

[42] “Optical properties of sapphire”. (2022). [Online]. Available: https://www.shinkosha.com/english/techinfo/feature/optical-properties-of-sapphire/.

[43] J. Burnett et al. “Intrinsic birefringence in calcium fluoride and barium fluoride”. *Physical Review B*. vol. 64, p. 241 102. 24 Nov. 2001. DOI: 10.1103/PhysRevB.64.241102.

[44] “Properties of fused silica”. (2020). [Online]. Available: https://www.heraeus.com/en/hca/fused_silica_quartz_knowledge_base_1/properties_1/properties_hca.html%5C#tabs-608478-7.

[45] “Ultraviolet lens assemblies”. (2020). [Online]. Available: https://www.universeoptics.com/uvlens_assemblies/.

[46] “Crystal material”. (2020). [Online]. Available: https://www.icc.ltd/category/crystal_material/.

[47] C. Zhang et al. “Low-loss metasurface optics down to the deep ultraviolet region”. *Light: Science & Applications*. vol. 9, p. 55. 1 Apr. 2020. DOI: 10.1038/s41377-020-0287-y.

[48] C. Zhang et al. “Tantalum pentoxide-based, all-dielectric ultraviolet metasurfaces”. Optica Publishing Group, 2020, FF3E.4. DOI: 10.1364/CLEO_QELS.2020.FF3E.4.

[49] K. Huang et al. “Ultraviolet metasurfaces of ≈80% efficiency with antiferromagnetic resonances for optical vectorial anti-counterfeiting”. *Laser & Photonics Reviews*. vol. 13, p. 1 800 289. 5 May 2019. DOI: 10.1002/lpor.201800289.

[50] "Design of aluminum nitride metalens in the ultraviolet spectrum". *Journal of Nanophotonics*. vol. 12, p. 1. 04 Jul. 2018. DOI: 10.1117/1.JNP.12.043513.

[51] N. Butt et al. "Realization of highly efficient trifocal metalens architecture with the blend of pancharatnam-berry and propagation phase effect". Z. Zhou et al., Eds. SPIE, Jan. 2023, p. 38. DOI: 10.1117/12.2644019.

[52] J. Kim et al. "Characteristics of peald–hafnium dioxide films and their application to gate insulator stacks of photosynaptic transistors". *Advanced Electronic Materials*. vol. 8, p. 2 101 061. 4 Apr. 2022. DOI: 10.1002/aelm.202101061.

[53] R. A. Rani et al. "Thin films and nanostructures of niobium pentoxide: Fundamental properties, synthesis methods and applications". *J. Mater. Chem. A*. vol. 2, pp. 15 683–15 703. 38 Jul. 2014. DOI: 10.1039/C4TA02561J.

[54] X. Gao et al. "Design of aln ultraviolet metasurface for single-/multi-plane holography". *Applied Optics*. vol. 59, p. 4398. 14 May 2020. DOI: 10.1364/AO.392799.

[55] Y. Deng et al. "All-silicon broadband ultraviolet metasurfaces". *Advanced Materials*. vol. 30, p. 1 802 632. 38 Sep. 2018. DOI: 10.1002/adma.201802632.

[56] J. Kim et al. "One-step printable platform for high-efficiency metasurfaces down to the deep-ultraviolet region". *Light: Science & Applications*. vol. 12, p. 68. 1 Mar. 2023. DOI: 10.1038/s41377-023-01086-6.

[57] C. Kittel. *Introduction to solid state physics*. 8th ed. Hoboken, NJ: Wiley, 2005.

[58] S. Uenoyama et al. "Monolithic integration of metalens in silicon photomultiplier for improved photodetection efficiency". *Advanced Optical Materials*. vol. 10, p. 2 102 707. 9 May 2022. DOI: 10.1002/adom.202102707.

[59] L. Guo et al. "Design of aluminum nitride metalens for broadband ultraviolet incidence routing". *Nanophotonics*. vol. 8, pp. 171–180. 1 Dec. 2018. DOI: 10.1515/nanoph-2018-0151.

[60] M. Hu et al. "Polarization-insensitive and achromatic metalens at ultraviolet wavelengths". *Journal of Nanophotonics*. vol. 13, p. 1. 03 Sep. 2019. DOI: 10.1117/1.JNP.13.036015.

[61] Z. Hu et al. "Ultrawide bandgap aln metasurfaces for ultraviolet focusing and routing". *Optics Letters*. vol. 45, p. 3466. 13 Jul. 2020. DOI: 10.1364/OL.395909.

[62] N. Mahmood et al. "All-dielectric trifunctional metadevices to efficiently structure ultraviolet light". Z. Zhou et al., Eds. SPIE, Jan. 2023, p. 37. DOI: 10.1117/12.2643990.

[63] S. Banerji et al. "Inverse designed achromatic flat lens operating in the ultraviolet". *OSA Continuum*. vol. 3, p. 1917. 7 Jul. 2020. DOI: 10.1364/OSAC.395767.

[64] M. Liu et al. "Polarization independent and broadband achromatic metalens in ultraviolet spectrum". *Optics Communications*. vol. 497, p. 127 182. Oct. 2021. DOI: 10.1016/j.optcom.2021.127182.

[65] M. L. Tseng et al. "Vacuum ultraviolet nonlinear metalens". *Science Advances*. vol. 8. 16 Apr. 2022. DOI: 10.1126/sciadv.abn5644.

[66] H. Ahmed et al. "Polarization insensitive all-dielectric metasurfaces for the ultraviolet domain". *Optical Materials Express*. vol. 10, p. 1083. 4 Apr. 2020. DOI: 10.1364/OME.387202.

[67] Z. Zhang et al. “High-efficiency all-dielectric metasurfaces for the generation and detection of focused optical vortex for the ultraviolet domain”. *Applied Sciences*. vol. 10, p. 5716. 16 Aug. 2020. DOI: 10.3390/app10165716.

[68] J. He et al. “Generating ultraviolet perfect vortex beams using a high-efficiency broadband dielectric metasurface”. *Optics Express*. vol. 30, p. 4806. 4 Feb. 2022. DOI: 10.1364/OE.451218.

[69] M. D. Shafqat et al. “Perfect vortex beam generation with high numerical aperture in broadband uv-visible regime”. Z. Zhou et al., Eds. SPIE, Jan. 2023, p. 41. DOI: 10.1117/12.2644784.

[70] N. Mahmood et al. “Ultraviolet–visible multifunctional vortex metaplates by breaking conventional rotational symmetry”. *Nano Letters*. vol. 23, pp. 1195–1201. 4 Feb. 2023. DOI: 10.1021/acs.nanolett.2c04193.

[71] B. Gholipour et al. “Reconfigurable ultraviolet and high-energy visible dielectric metamaterials”. *Nano Letters*. vol. 19, pp. 1643–1648. 3 Mar. 2019. DOI: 10.1021/acs.nanolett.8b04576.

[72] T.-A. Chen et al. “Tio ₂ nanodisk arrays as all-dielectric huygens’ metasurfaces for engineering the wavefront of near-uv light”. *ACS Applied Nano Materials*. vol. 5, pp. 925–930. 1 Jan. 2022. DOI: 10.1021/acsanm.1c03585.

[73] T. Siefke et al. “Materials pushing the application limits of wire grid polarizers further into the deep ultraviolet spectral range”. *Advanced Optical Materials*. vol. 4, pp. 1780–1786. 11 Nov. 2016. DOI: 10.1002/adom.201600250.

[74] K.-H. Kim et al. “Dielectric huygens’ metasurfaces with diverse functionalities in the range from near-uv to deep-uv”. *Optics Communications*. vol. 493, p. 126 993. Aug. 2021. DOI: 10.1016/j.optcom.2021.126993.

[75] R. M. A. Azzam et al. *Ellipsometry and polarized light*. Amsterdam ; New York : New York: North-Holland Pub. Co. ; sole distributors for the U.S.A. and Canada, Elsevier North-Holland, 1977.

[76] E. D. Palik, Ed. *Handbook of optical constants of solids II*. Boston: Academic Press, 1991.

[77] Z. Cui. *Nanofabrication*. Springer US, 2008. DOI: 10.1007/978-0-387-75577-9.

[78] A. A. Tseng, Ed. *Nanofabrication: fundamentals and applications*. Singapore ; Hackensack, N.J: World Scientific, 2008.

[79] T. I. Awan et al. *Chemistry of nanomaterials: fundamentals and applications*. Amsterdam, Netherlands ; Cambridge, MA: Elsevier, 2020.

[80] J. Green. “Advantages and disadvantages of ion beam sputtering”. (2023). [Online]. Available: https://www.sputtertargets.net/advantages-and-disadvantages-of-ion-beam-sputtering.

[81] P. M. Martin. *Handbook of deposition technologies for films and coatings: science, applications and technology*. 3rd ed. Amsterdam: Elsevier, 2010.

[82] J. Lu et al. “Atomic layer deposition—sequential self-limiting surface reactions for advanced catalyst “bottom-up” synthesis”. *Surface Science Reports*. vol. 71, pp. 410–472. 2 Jun. 2016. DOI: 10.1016/j.surfrep.2016.03.003.

[83] R. M. Pinto et al. “Piezoelectric aluminum nitride thin-films: A review of wet and dry etching techniques”. *Microelectronic Engineering*. vol. 257, p. 111 753. Mar. 2022. DOI: 10.1016/j.mee.2022.111753.

[84] S. Norasetthekul et al. “Etch characteristics of hfo2 films on si substrates”. *Applied Surface Science*. vol. 187, pp. 75–81. 1-2 Feb. 2002. DOI: 10.1016/S0169-4332(01)00792-9.

[85] T. P. Coleman et al. “≪title>plasma etching of chromium films in the fabrication of photomasks</title>”. G. V. Shelden et al., Eds. Oct. 1995, pp. 62–72. DOI: 10.1117/12.228216.

[86] Y. Suzuki et al. “Gas plasma etching of chromium films”. *Japanese Journal of Applied Physics*. vol. 21, p. 1328. 9R Sep. 1982. DOI: 10.1143/JJAP.21.1328.

[87] “Positive pmma e-beam resists ar-p 630 – 670 series”. (2014). [Online]. Available: https://www.allresist.com/wp-content/uploads/sites/2/2015/12/allresist_produktinfos_ar-p630-670_englisch.pdf.

[88] “Ar 300-80 new and hmds adhesion promoter”. (2021). [Online]. Available: https://www.allresist.com/wp-content/uploads/sites/2/2021/02/Allresist_Product-information_Adhesions-Promoter_AR-300-80new_HMDS_English_web.pdf.

[89] “Ar-p 6200 e-beam resists with highest resolution”. (2019). [Online]. Available: https://www.allresist.com/wp-content/uploads/sites/2/2020/03/AR-P6200_CSAR62english_Allresist_product-information.pdf.

[90] “Ar-p 617 e-beam resists for nanometer lithography”. (2019). [Online]. Available: https://www.allresist.com/wp-content/uploads/sites/2/2020/03/AR-P610_english_Allresist_product-information.pdf.

[91] “Protective coating pmma electra 92 (ar-pc 5090)”. (2016). [Online]. Available: https://www.allresist.com/wp-content/uploads/sites/2/2022/05/Allresist_Product-information-Protective-Coating-AR-PC-5090_5091-English-web.pdf.

[92] “Technietch cr01”. (2022). [Online]. Available: https://www.microchemicals.com/products/etching_mixtures/technietch_cr01chromium_etchant.html.

[93] “He-cd laser”. (2022). [Online]. Available: https://www.kimmon.com/english/products/hecd.html.

[94] “High-power microspot® focusing objectives for uv lasers”. (2023). [Online]. Available: https://www.thorlabs.com/newgrouppage9.cfm?objectgroup_id=3271%5C&pn=LMU-40X-NUV.

[95] “Kymera 193i manual”. (2019). [Online]. Available: https://andor.oxinst.com/downloads/uploads/Kymera_193i_Manual.pdf.

[96] “Newton emccd”. (2023). [Online]. Available: https://andor.oxinst.com/assets/uploads/products/andor/documents/andor-newton-emccd-specifications.pdf.

[97] I. Gablech et al. “Preparation of high-quality stress-free (001) aluminum nitride thin film using a dual kaufman ion-beam source setup”. *Thin Solid Films*. vol. 670, pp. 105–112. Jan. 2019. DOI: 10.1016/j.tsf.2018.12.035.

[98] “Ar-n 7520 e-beam resists for mix & match”. (2019). [Online]. Available: https://www.allresist.com/wp-content/uploads/sites/2/2022/03/Allresist_Product-information-E-Beamresist-AR-N-7520-English-web.pdf.

[99] R. Armstrong et al. “Creation of regular arrays of faceted AlN nanostructures via a combined top-down, bottom-up approach”. *Journal of Crystal Growth*. vol. 548, p. 125 824. Oct. 2020. DOI: 10.1016/j.jcrysgro.2020.125824.

[100] L. Shen et al. “Synthesis of single-crystalline wurtzite aluminum nitride nanowires by direct arc discharge”. *Applied Physics A*. vol. 84. no. 1-2, pp. 73–75. May 2006. DOI: 10.1007/s00339-006-3580-6.

[101] S.-C. Shi et al. “Structural evolution of AlN nano-structures: Nanotips and nanorods”. *Chemical Physics Letters*. vol. 418. no. 1-3, pp. 152–157. Jan. 2006. DOI: 10.1016/j.cplett.2005.10.107.